AGU ADVANCING EARTH AND SPACE SCIENCE

Water Resources Research

RESEARCH ARTICLE

10.1029/2021WR030891

Key Points:

- Experimental results from four cycles of CO_2 and brine injections into Bentheimer sandstone
- X-ray tomography imaged data exhibit evolution of fluid configuration and wettability state
- Transition to "patchy" mixed-wet state increases residual trapping of CO_2

Supporting Information:

Supporting Information may be found in the online version of this article.

Correspondence to:

A. L. Herring,
annalisaherring@gmail.com

Citation:

Herring, A. L., Sun, C., Armstrong, R. T., Li, Z., McClure, J. E., & Saadatfar, M. (2021). Evolution of Bentheimer sandstone wettability during cyclic $scCO_2$-brine injections. *Water Resources Research*, *57*, e2021WR030891. https://doi.org/10.1029/2021WR030891

Received 22 JUL 2021
Accepted 2 NOV 2021

Author Contributions:

Conceptualization: A. L. Herring
Formal analysis: A. L. Herring, C. Sun, R. T. Armstrong
Funding acquisition: A. L. Herring
Investigation: A. L. Herring, Z. Li, M. Saadatfar
Methodology: A. L. Herring
Project Administration: A. L. Herring
Software: J. E. McClure
Writing – original draft: A. L. Herring
Writing – review & editing: C. Sun, R. T. Armstrong, Z. Li, J. E. McClure, M. Saadatfar

Evolution of Bentheimer Sandstone Wettability During Cyclic $scCO_2$-Brine Injections

A. L. Herring[1], C. Sun[2], R. T. Armstrong[3], Z. Li[1,4], J. E. McClure[4], and M. Saadatfar[1,5]

[1]Research School of Physics, The Australian National University, Canberra, ACT, Australia, [2]State Key Laboratory of Petroleum Resources and Prospecting, China University of Petroleum, Beijing, China, [3]School of Minerals and Energy Resources Engineering, University of New South Wales, Sydney, NSW, Australia, [4]Advanced Research Computing, Virginia Polytechnic Institute & State University, Blacksburg, VA, USA, [5]School of Civil Engineering, The University of Sydney, Sydney, NSW, Australia

Abstract Geologic sequestration in sedimentary formations has been identified as a potential technology to prevent climate-change inducing carbon dioxide (CO_2) from being emitted to the atmosphere. To achieve safe and effective storage underground, accurate understanding, and predictions of supercritical CO_2 ($scCO_2$) behavior in subsurface rock formations is required; including quantifying how much $scCO_2$ is trapped within pore spaces by capillarity (vs. how much remains mobile), and constraining the occurrence of physio-chemical reactions between $scCO_2$ and the mineral matrix. Experiments where multiple cycles of $scCO_2$ and brine are injected into rock samples have produced conflicting results regarding the consistency of trapping as cycles progress; likely due to differences in mineral content, pressure-temperature conditions, aqueous chemistry parameters, and experimental setups. We present a new set of experiments, replicating the conditions of a previous study, but with a new experimental design, apparatus, and timeline. We confirm previous results that demonstrated shifts in injection pressure and $scCO_2$ trapping behavior over multiple injection cycles, and we conduct additional analyses to discern the fluid-fluid macroscopic contact angle, interface mean and Gaussian curvatures, $scCO_2$ interfacial area, and topology of trapped $scCO_2$ ganglia. We also performed lattice-Boltzmann simulations approximating experimental conditions where solid wettability was systematically altered over multiple injections cycles; trends in $scCO_2$ ganglia characteristics compare well between experiment and simulation. The results indicate that this system undergoes a transition to a "patchy" mixed-wet state, and we observe that this wettability alteration renders $scCO_2$ more stable in the rock pore space, increasing capillary trapping over four injection cycles.

1. Introduction

Almost all scenarios that limit climate-change-caused temperature rise to ≤2°C rely on large-scale geologic sequestration to redirect carbon dioxide (CO_2) emissions away from the atmosphere and instead into underground storage (IPCC, 2014, 2019). Geologic sequestration is being considered both as a way to prevent carbon emissions from large point source polluters (e.g., fossil fuel energy production, cement manufacturers), and also as a potential negative emissions technology when coupled with bioenergy with carbon capture and storage, or direct air capture (Bui et al., 2018; IEA, 2020; IPCC, 2005, 2019). The short-term (i.e., order of decades) security of a geologic sequestration operation in a sedimentary formation relies on two physical mechanisms: (a) the presence of a sound impermeable caprock to enable "structural" trapping of the relatively buoyant CO_2 plume below the caprock (Shukla et al., 2010; Song & Zhang, 2013), and (b) the interfacial interactions between rock-CO_2-resident brine which break off small bubbles of disconnected CO_2 within the pore structure of the rock formation, termed "capillary" or "residual" trapping (Abidoye et al., 2015; Boot-Handford et al., 2014; Burnside & Naylor, 2014; Krevor et al., 2015). Provided that these mechanisms hold the CO_2 underground for sufficient time, the CO_2 will dissolve into the surrounding formation water and subsequently undergo mineralization processes (De Silva et al., 2015), trapping the carbon in stable nongaseous forms on geologic timescales. Geologic reservoirs targeted for sequestration are at depths such that the reservoir pressure dictates that the density of the CO_2 phase is relatively high (although still less than the resident brine), enabling more efficient storage; this is usually accompanied by geothermal gradients that force the CO_2 into a supercritical state, denoted here as "$scCO_2$."

Many recent studies have focused on capillary trapping because it is a more secure storage mechanism than structural trapping alone. Capillary trapping of $scCO_2$ breaks up the larger $scCO_2$ plume, holding $scCO_2$ bubbles in individual pore bodies within the rock architecture. This disperses the injected $scCO_2$ over a larger volume, decreasing the size of the mobile connected plume and the associated risk of plume migration in the event of caprock failure. Capillary trapping occurs in multiphase fluid-porous medium systems when there is a local (order of individual pore bodies and throats) or global (on the order of a representative elementary volume) increase in the volume fraction ("saturation") of the more wetting fluid (for water-wet systems, the wetting fluid is water or an aqueous solution, and $scCO_2$ is a nonwetting phase). This causes the wetting phase to spread over the surface of the rock, and allows films of the wetting phase to grow and merge at constrictions within the rock structure (pore throats), thus "snapping off" and surrounding small bubbles ("ganglia") of nonwetting phase fluid (Roof, 1970). Snap-off processes can occur under many different flow conditions, including during nonwetting phase injection ("drainage"; Andrew et al., 2015; Herring, Gilby, et al., 2018) and during wetting phase injection ("imbibition"; Deng et al., 2015; Mahmud & Nguyen, 2006; Singh et al., 2017) as long as the pore-scale reconfigurement of fluids allows for an increase of wetting phase at crucial locations within the porous media. Many studies have investigated how capillary trapping levels are enhanced or suppressed in different medium geometries (Andersson et al., 2018; Herring et al., 2019; Mahmud & Nguyen, 2006; Mansoori et al., 2009; Pentland et al., 2010; Tanino & Blunt, 2012), through manipulation of fluid and flow properties (Bachu, 2003; Bachu et al., 2009; Bennion & Bachu, 2013; Herring et al., 2015; Kimbrel et al., 2015; Nguyen et al., 2006; Wildenschild et al., 2011), and in different rock types (Bachu, 2015; Burnside & Naylor, 2014; Tanino & Blunt, 2012; Wang & Tokunaga, 2015). A review by Krevor et al. (2015) compiled results of many drainage-imbibition experiments, demonstrating that capillary trapping of $scCO_2$ in these experimental systems is dependent on the initial $scCO_2$ saturation and generally follows the curve described by the Land model (Land, 1968) for both sandstones and carbonates.

The current study is motivated by an inconsistency in the literature regarding whether cyclic drainage-imbibition injections increase residual trapping. Most of the experimental studies included in the Krevor et al. (2015) review looked at one drainage-imbibition cycle (El-Maghraby & Blunt, 2013; Krevor et al., 2012; Lu et al., 2013; Shi et al., 2011; Zuo & Benson, 2014); or multiple cycles, but where the core was depressurized and/or flooded with unsaturated brine to return the core to an original 100% brine-saturated state (Akbarabadi & Piri, 2013, 2015; Li et al., 2015; Niu et al., 2015; Pentland et al., 2011). There are relatively fewer studies that have looked at sequential drainage-imbibition studies. Herring et al. (2016) conducted an experimental study investigating cyclic injection behavior of $scCO_2$ and brine under supercritical conditions, but relatively low pressure (8.6 MPa/1250 PSI) and temperature (40°C). The results of that study indicated a competition during cycling between increased trapping (which the authors attributed to an unidentified surface geochemical/wettability alteration process) and decreased trapping due to increasing connectivity of the $scCO_2$ phase (a previously identified mechanism Herring et al., 2013, 2015; Schlüter et al., 2016). Additional analysis of the Herring et al. (2016) data set showed that the topology and morphology of individual residual $scCO_2$ ganglia also changed over the course of the injection cycles, leading to larger and more interconnected residual ganglia, invading smaller pore throats (Herring, Wildenschild, et al., 2018). The trend of increasing residual saturation over consecutive drainage-imbibition cycles has also been observed in Bentheimer and Nugget sandstones at 12.4 MPa and 45°C (Dalton et al., 2020). Similarly, experiments by Edlmann et al. (2019) monitored pressure signals over six CO_2-water injection cycles (carried out under similar pressure-temperature conditions as Herring et al., 2016) and found increased differential pressure, associated with increased residual trapping of $scCO_2$, for each subsequent cycle. Abdoulghafour et al. (2020) investigated drainage capillary pressures for $scCO_2$ systems and found that the secondary drainage achieved a higher capillary pressure and higher $scCO_2$ saturation than the primary drainage, and stated that the higher $scCO_2$ saturation was due to "CO_2 cluster coalescence in the pore space during the second CO_2 injection," a finding that supports previous imaging studies (Dalton et al., 2020; Herring, Wildenschild, et al., 2018). Capillary pressure-saturation measurements of drainage-imbibition cycles in unconsolidated media have indicated that the wettability of quartz sand is altered to CO_2-wetting under supercritical conditions (Plug & Bruining, 2007), and for consecutive drainage-imbibition flows, a transition in wettability occurs over time/cycle number due to $scCO_2$ exposure for quartz and carbonate sands (Tokunaga et al., 2013; Wang & Tokunaga, 2015). Furthermore, Tokunaga et al. (2013) and Wang and Tokunaga (2015) observed elevated residual trapping of $scCO_2$ relative to air in these sands, despite capillary pressure measurements indicating shifts toward $scCO_2$-wetting behavior under supercritical conditions. These studies indicate that the $scCO_2$-brine-solid system evolves over multiple cycles of $scCO_2$ and brine injections.

In contrast, Ruprecht et al. (2014) conducted three drainage and imbibition cycles using a co-flooding fractional flow set-up at 9 MPa and 50°C in a fired Berea sandstone sample and found good agreement over sequential cycles with the Land model, indicating no significant change in rock properties over the course of the cycles. Similarly, Saeedi and Rezaee (2012) investigated cyclic injections at relatively high pressure (17.8 MPa/2580 PSI) and temperature (80°C) conditions and observed that there was no significant change in the amount of residual trapping or other flow characteristics over the course of four cycles; and another study using nitrogen gas as a CO_2 proxy showed that fractional pore volume water-alternating-gas injections actually reduced residual gas trapping (Adeoye et al., 2017). Garing and Benson (2019) measured capillary pressure-saturation relationships for $scCO_2$-water floods in unfired Berea sandstone cores, and then repeated the measurements after firing the cores, and again after exposing the core to $scCO_2$ for 28 days; and observed no significant difference between the three sets of measurements. The Ruprecht et al. (2014) and Saeedi and Rezaee (2012) findings are more consistent with traditional multiphase theory (e.g., as described in Raeesi et al., 2014), and smooth initial-residual trapping relationships are currently assumed in larger-scale modeling studies; for example, Rasmusson et al. (2016). The determination of whether the $scCO_2$-brine-rock system exhibits evolutionary behavior over the course of multiple cycles, and the mechanism and system parameters that enable this behavior, is thus crucial for predicting and engineering the long-term behavior of subsurface $scCO_2$ at injection sites.

Recently, some potential mechanisms have been identified in $scCO_2$-brine systems which might be responsible for the anomalous behavior described above. Fines migration describes the dissolution and mobilization of small particulates of quartz, intergranular clays, or other minerals during core flooding; these "fines" may then be re-deposited on rock grain surfaces or potentially block small pore throats, leading to permeability reduction (a.k.a. "formation damage", Galal et al., 2016; Muecke, 1979). Fines migration is dictated by factors influencing the interfacial forces on particulates, including fluid pH and salinity (and particularly the presence of divalent cations) and mineral wettability (Jones, 1964; Khilar & Fogler, 1983; Mungan, 1965; Zhang et al., 2020). Evidence of fines migration has been observed in Berea sandstones as a result of core flooding with $scCO_2$-saturated brine (Ge et al., 2020; Othman et al., 2019); a companion study (Zhang et al., 2020) indicated that the mineral phases kaolinite, chlorite, and muscovite exhibited physical and/or chemical changes after exposure to $scCO_2$-saturated brine and were most likely to be mobilized (in contrast to quartz and microcline, a potassium-rich feldspar, which showed no changes upon exposure). Ge et al. (2020) and Zhang et al. (2020) suggest that a primary impact of fines migration is the mobilization of fines and subsequent blockage of pore throats, leading to reduced permeability. In a more recent study, Ge et al. (2022) also found that fines migration increased residual saturation of $scCO_2$; the authors attribute this effect also to pore throat blockage. Even in the absence of fines migration, the wettability of clay minerals can have a significant impact on relative permeability endpoints and subsequent trapping of $scCO_2$ (Fan et al., 2020). The Bentheimer sandstone cores investigated by Herring et al. (2016) and further herein are largely comprised of quartz, but are unfired with K-feldspar and kaolinite present; so there is potential for clays to influence flow, and for fines migration (especially with respect to kaolinite) to occur.

Another potential surface chemistry impact is wettability alteration of the quartz/silica surfaces upon exposure to $scCO_2$. Wettability characterization of minerals in the presence of $scCO_2$ and CO_2-saturated brine is a source of disagreement in the literature; quartz is often assumed to maintain its strongly water-wetting properties, but numerous studies indicate that this assumption may not be correct (e.g., see review by Iglauer, 2017). Wan et al. (2014) provide a review of contact angle measurements on mica and possible sources of conflict in contact angle measurements, including: minor differences in sample preparation, contact order (i.e., whether the first substrate contact was by brine or $scCO_2$), contact time, and number of incidences of $scCO_2$-substrate contacts. Increases in system pressure, brine salinity, and impurities in fluids increase contact angle (away from water-wetting; Iglauer, 2017). Dewetting of smooth silica surfaces in the presence of $scCO_2$ has been observed directly in micromodel experiments (Kim et al., 2012). Adhesion of CO_2 to solid surfaces (with accompanying increases in contact angle) has been well-documented for smooth glass (Dickson et al., 2006) and some mineral (Wan et al., 2014) surfaces; and it has been suggested that adhesion of $scCO_2$ molecules to surfaces in geologic samples may render $scCO_2$ stable during displacement and increase residual trapping (Wang, Tao, et al., 2013). CO_2 adhesion is known to be influenced by pH (a function of $scCO_2$ solubility, and therefore pressure-temperature conditions), wetting phase ionic strength, and surface roughness (Chiquet et al., 2007; Jung & Wan, 2012; Wang, Edwards, & Clarens, 2013; Wang, Tao, et al., 2013); this indicates that different pressure-temperature conditions or different fluid-rock systems will result in conflicting emphasis on this effect. There are hysteretic and temporal dependencies to the adhesion process as demonstrated by the behavior of CO_2-water contact angles on glass slides (Dickson et al., 2006) and silica surfaces/powders/films (McCool & Tripp, 2005) during pressurization-depressurization cycles. In the experiments of Dickson et al. (2006), contact angles were observed to increase during pressurization, and decrease during depressurization, but the values measured during depressurization were consistently more CO_2-wet than those measured at the equivalent pressure during pressurization; the authors suggest that adhesion of CO_2 occurs rapidly, but slowly reverses. A return to the original contact angles of the surfaces required a week after depressurization for intermediate-wet surfaces (Dickson et al., 2006), and a full month for hydrophilic mesoporous surfaces (McCool & Tripp, 2005). We note that quartz and rough surfaces have been observed to be less susceptible to adhesion than smooth silica (Wang, Tao, et al., 2013), potentially limiting the impact of adhesion in real geologic systems.

In the current study, we provide new experimental evidence of a series of four consecutive drainage-imbibition cycles with $scCO_2$ and 1.0 M potassium-iodide brine in a Bentheimer sandstone core, conducted under similar pressure-temperature conditions as Herring et al. (2016); but in a different experimental apparatus with different flow directions, different imaging protocol, and under different duration than those previous experiments. Even with the differences in experimental system set-ups, we demonstrate that this experiment supports the previously observed phenomenon of increasing residual trapping for cyclic $scCO_2$-brine injections; and further, we show that macroscopic (per-ganglia) contact angle distributions shift toward $scCO_2$-wetting conditions as cycle number increases, indicating a transition to a "patchy" mixed-wet state. Trends in $scCO_2$ ganglia characteristics compare well to the results of lattice-Boltzmann (LB) simulations where solid wettability was altered systematically over multiple drainage-imbibition cycles. The results are discussed in the context of the two potential wettability alteration mechanisms described above.

These results suggest that in regions geologic storage formations undergoing multiple drainage-imbibition cycles, capillary trapping of $scCO_2$ may be higher than previously suggested. The results also indicate that it may be possible to enhance residual trapping in certain geologic-pressure-temperature settings.

2. Materials and Methods

2.1. Experimental Setup

Experiments were conducted via a high pressure, high-temperature triaxial flow cell installed within a laboratory-scale helical X-ray microcomputed tomography (CT) imaging instrument at the Australian National University CTLab, allowing the entire month-long experimental run to be conducted in situ; some system specifications have been previously reported (Øren et al., 2019). The flow cell was constructed of aviation grade aluminum alloy (T7000 series) and utilizes an internal Linear Variable Differential Transformer ("LVDT"; Solartron Metrology) to monitor vertical core displacement and maintain constant axial stress during injections. Two hydraulic oil pumps (Metarock Laboratories) control radial confining and axial fluid pressure, and two Hastelloy pumps (Teledyne ISCO) control injection fluids. Stainless steel flow lines connect immobile components (e.g., pumps, valve panel, fluid mixer), and PEEK fluid lines connect the mobile flow cell (installed on the sample stage within the X-ray CT instrument) to the pumps and effluent back-pressure regulator. All injection fluids were introduced at the bottom of the core, combined effluent exited from the top. The fluid mixing vessel relies on gravity separation, with ports at the top and bottom to allow extraction of low/high-density fluids, and a sight window (BOROFLOAT® 33 Borosilicate Glass) was used to monitor fluid levels. The mixer was placed on a standard laboratory magnetic stirrer/heat pad, this facilitated vigorous mixing of fluids and provided temperature control; additional heating elements were incorporated in walls of the mixer to ensure stable temperature control throughout the vessel. In addition, the flow cell, fluid injection pumps, valve panel, and PEEK flow lines are all insulated/temperature-controlled; for this experiment, the temperature was maintained at 40°C.

A Bentheimer sandstone core, 12 mm in diameter and 36 mm tall, was bounded by porous sintered copper flow diffusers (to extend the porous matrix and prevent capillary end effects) and stainless steel end-caps on both ends and encased in shrinkwrap. O-rings were set on the endcaps and the core assembly was placed in the flow cell. The upper cap (outlet end) of the flow cell was then affixed to the cell and the upper floating piston was screw-tightened until the internal LVDT signaled vertical movement of the core of ≥1 μm, indicating that the core assembly was flush against both upper and lower pistons. Axial pressure was then ramped up to 0.7 MPa/100 PSI; pressurization was conducted using X-ray radiograph live imaging to ensure adequate compression of O-rings and confirm structural integrity of the sandstone core. Radial confining oil was then pumped to fill the region external to the core assembly, and then to increase the confining pressure on the core; the axial pressure was simultaneously increased at a rate that maintained a constant LVDT position. X-ray radiograph live-imaging was used throughout to manually check the pressurization process and to confirm no leakage of confining oil into the core.

The "dry" scan of the core was completed under radial confining pressure of 3.4 MPa/500 PSI. After the dry scan had completed, gaseous CO_2 was flushed through the core to displace the air that was present, and then "dead" (i.e., not mixed with $scCO_2$) 1.0 M potassium iodide (KI) brine was pumped through the core at high flow rate (2–5 ml/min). Radial confining pressure, axial pressure, and pore pressure were all simultaneously elevated (again, while maintaining a constant LVDT position and with visual monitoring via X-ray radiograph live-imaging) to working pressure: pore pressure of 8.6 MPa/1250 PSI, radial confining pressure of 10.3 Mpa/1500 PSI. A low-resolution scan (voxel size 19.7 μm) was acquired to ensure complete saturation of the core at this pressurized state; after this, the core was flushed again at low flow rate (0.05 ml/min) with 25 ml $scCO_2$-saturated 1.0 M KI brine (this "live" brine had been mixed with $scCO_2$ under working temperature and pressure for >48 h), and another low-resolution scan was acquired to again confirm complete saturation of the core with brine. At this point, drainage ($scCO_2$ injection)-imbibition (brine injection) cycles commenced, with radiograph-based time-lapse sequences acquired during pumping and a full 3D high-resolution Region-of-Interest ("ROI") scan (Huang et al., 2021; Latham et al., 2008, 2018; Myers et al., 2011) acquired at the endpoint of every flow process (i.e., after cessation of flow and at least one hour of equilibration time). The imbibition flow rate was chosen to approximate the capillary number of the experiments of Herring et al. (2016), assuming the conventional macroscopic definition $Ca = \frac{\mu \times v}{\sigma}$; where μ is the invading fluid viscosity, v is the invading fluid interstitial velocity, and σ is the $scCO_2$-brine interfacial tension; note that this corresponds to a relatively high injection flow rate for a geologic injection. Volume, flow rate, scan properties, and nomenclature details for each stage of the experiment are provided in Table 1.

2.2. 3D X-Ray CT Data Processing and Morphological Phase Characterization

The raw gray scale tomographic data volumes for all S_I ("initial", postdrainage) and S_R ("residual", post-imbibition) scans were first registered to the dry tomographic data set to allow direct and precise comparison of phase distributions in each data set. Data volumes were cropped to a central region, and gray scale intensity variation (due to beam hardening and attenuation distortion due to high-density flow diffusers at the core ends) was corrected in radial and vertical directions. The dry scan was segmented into three phases (pore, solid grains, and clays) using converging active contours "CAC") segmentation routines (Sheppard et al., 2004). Four-phase segmentation ($scCO_2$, brine, solid grains, and clays) was accomplished by overlaying the phase-labeled dry data set on all the registered S_I and S_R data volumes, and performing a final additional CAC routine to distinguish between $scCO_2$ and brine, only on the regions labeled "pore" in the dry data set (e.g., Figure 1c). The CAC thresholds were consistently calculated for each S_I and S_R data volume based on the positions of "peaks" in the gray scale histograms as measured for each tomogram. Speckle noise removal was accomplished by removing $scCO_2$-labeled clusters smaller than 268 voxels (equivalent to a sphere with a radius of 15.0 μm), and also by removing any isolated inclusions from within the $scCO_2$ phase. The final data volumes used for quantitative analysis were cylinders with a diameter of 8.14 mm and a height of 27.3 mm, equivalent to a physical volume of 1,420 mm^3 (or 2.69×10^{10} voxels); and had an image-based porosity of 21.3% (consistent with laboratory measurements of Bentheimer sandstone (Peksa et al., 2015, 2016). Calculation of $scCO_2$ volumes and pore space occupancy characteristics was performed for all S_I and S_R scans; detailed morphological analysis was performed for S_R scans, including interfacial areas with rock and brine phases (Ohser & Mücklich, 2001), and $scCO_2$-brine interface curvatures and $scCO_2$ topological metrics as described further below.

Table 1
Experimental, Lattice-Boltzmann (LB) Simulation, and Imaging Parameters

Experimental system properties

Parameter	Value
Pore pressure	8.6 MPa/1250 PSI
Radial confining pressure	10.3 MPa/1500 PSI
Temperature	40°C
Drainage flow rate	0.388 ml/min
Imbibition flow rate	0.388 ml/min
Pore volume	0.87 ml
X-ray energy	120 keV
X-ray current	60 µA
ROI scans	
Voxel size	3.75 µm
Scan time	22.2 hrs
Field of view (*x*, *y*, *z*)	10.8, 10.8, 32.5 mm
Low-res scans	
Voxel size	19.7 µm
Scan time	2.6 hrs
Field of view (*x*, *y*, *z*)	27.5, 27.5, 33.0 mm

Fluid and flow properties

Parameter	Experimental	LB simulation
$scCO_2$ viscosity	0.03 mPa-s	-
Brine viscosity	0.65 mPa-s[a]	-
Viscosity ratio	0.05	0.2
Interfacial tension	≈35 mN/m[b]	30 mN/m
Imbibition capillary number	$10^{-5.3}$	10^{-4}

Imaging sequence

Process	Injection details	Scan label	Scan type
Dry scan		Dry	ROI
Original saturation	180 ml dead brine	$S_{O,D}$	Low-res
Original saturation	25 ml live brine	$S_{O,L}$	Low-res
Drainage 1	44 ml $scCO_2$	$S_{I,1}$	ROI
Imbibition 1	25 ml live brine	$S_{R,1}$	ROI
Drainage 2	25 ml $scCO_2$	$S_{I,2}$	ROI
Imbibition 2	25 ml live brine	$S_{R,2}$	ROI
Drainage 3	25 ml $scCO_2$	$S_{I,3}$	ROI
Imbibition 3	25 ml live brine	$S_{R,3}$	ROI
Drainage 4	25 ml $scCO_2$	$S_{I,4}$	ROI
Imbibition 4	25 ml live brine	$S_{R,4}$	ROI

Note. ROI, region-of-interest.
[a]Approximated based on viscosity of pure water at 40°C. [b]Interpolated from Bachu and Bennion (2008).

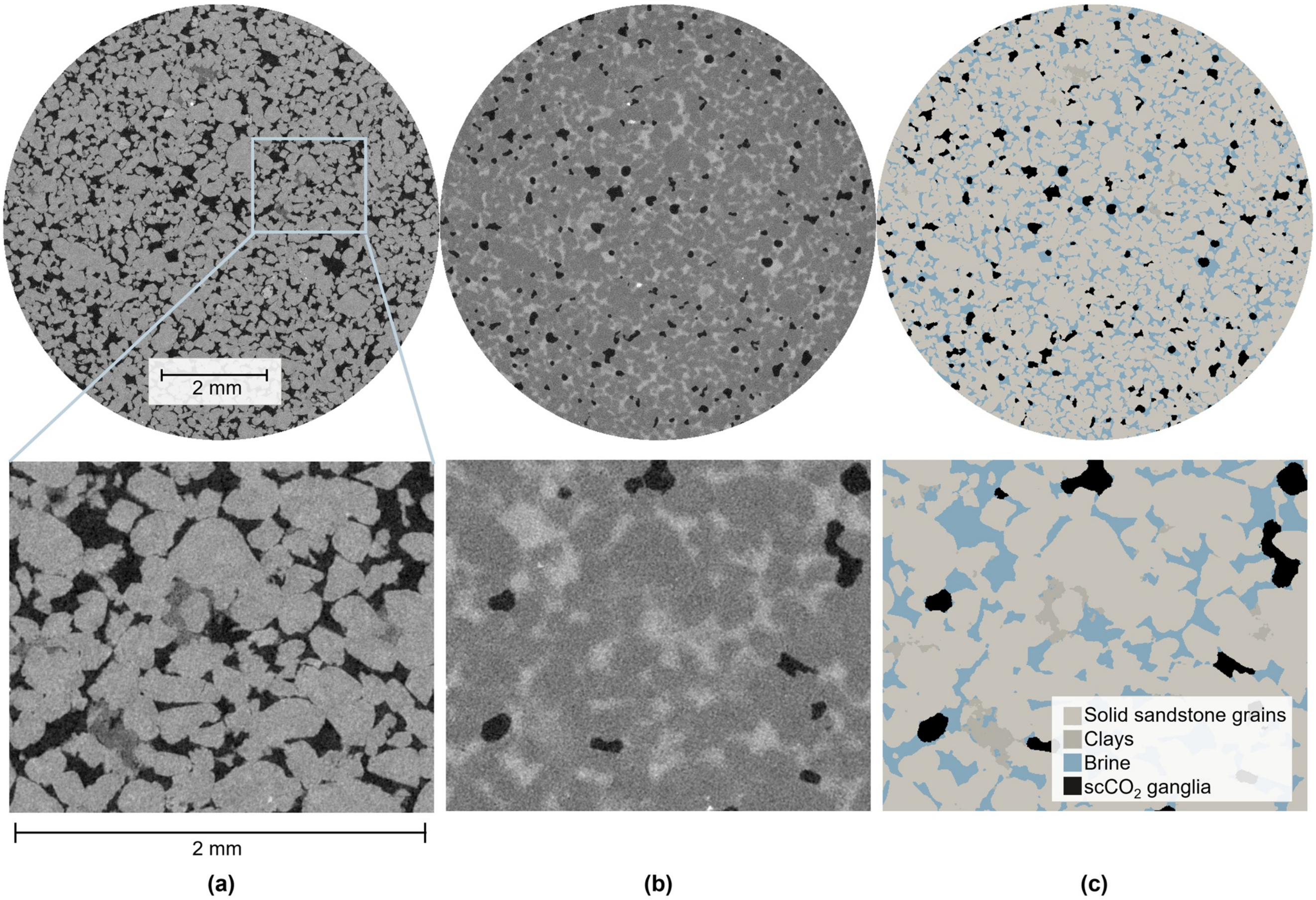

Figure 1. Example of X-ray computed tomography (CT) data combination and processing; illustrated by 2D cross-sectional slices (top row) and zoomed-in regions (bottom row). Tomograms of the dry sample (a) and the sample after three drainage-imbibition cycles with scCO$_2$ and brine, $S_{R,3}$, (b) were aligned. The phase-labeled data for the dry data set was overlain on the $S_{R,3}$ tomogram, and the scCO$_2$ and brine phases were then labeled and denoised to produce the four-phase "segmented" $S_{R,3}$ data volume (c) that provides the basis for quantitative measurements.

To measure interface curvatures, we follow the protocol described by Herring et al. (2017): the segmented data was used to identify the locations of scCO$_2$-brine interfaces and map them back to the original tomograms, then, curvatures were measured at cloud points generated from the gradient of gray scale intensities at those interface locations. Cloud points within a distance of two voxels from the solid surface were neglected, and cloud points farther from the solid surface within a given cloud were given a higher weighting; these constraints help reduce errors associated with imaging deficiencies and artifacts at the three-phase contact line. The mean curvature of the interface (κ) was calculated as the average of the two principle curvatures of the interface.

The topology of the scCO$_2$ ganglia in S_I and S_R scans was quantified for $1,500^3$ voxel subsections of the data via persistent homology analysis using the open-source program Diamorse (Delgado-Friedrichs et al., 2015). This analysis provides quantification of topological features (e.g., β_0, the number of isolated components, and β_1, the number of loops or redundant interconnections within the scCO$_2$ ganglion, β_2 the number of inclusions or holes within a phase) as well as the critical length scales of these features (Herring et al., 2019; Robins et al., 2015). In this analysis, we focus on the number and size characteristics of the β_1 loops formed by the scCO$_2$ phase after drainage and imbibition.

2.3. Deficit Curvature and Macroscopic Contact Angle Analysis

Characterization of the macroscopic wettability state of the sample after successive drainage-imbibition cycles was accomplished via calculation of deficit curvature (Sun, McClure, Mostaghimi, Herring, Berg,

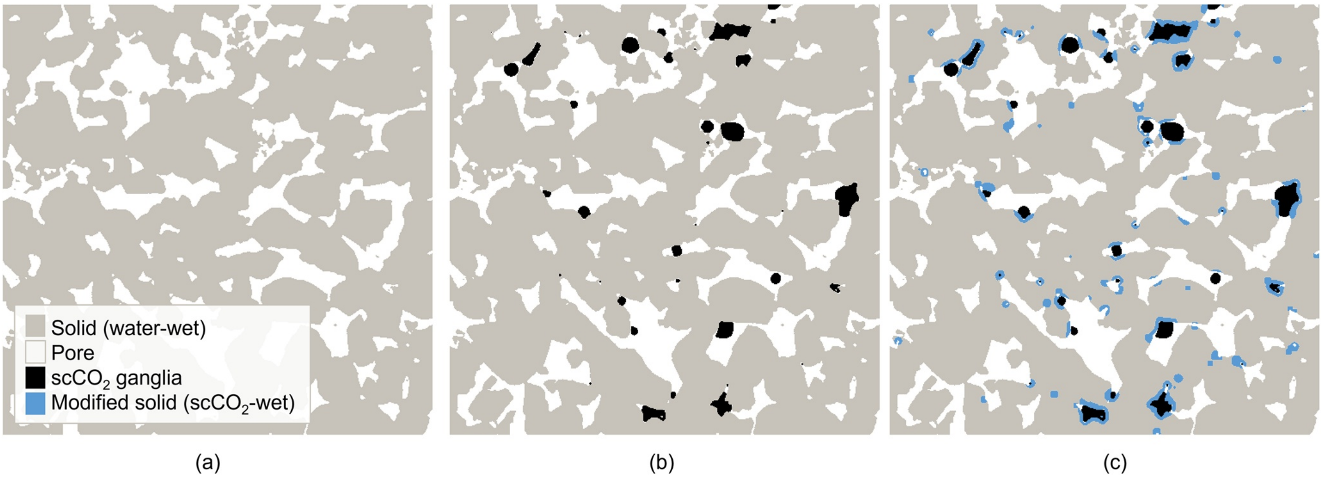

Figure 2. 2D Slices from 3D subset comprising the lattice-Boltzmann simulation domain. The initial drainage-imbibition cycle was simulated in the 3D sandstone geometry comprised of pore space and water-wet (contact angle of 55°) solid sandstone (a), resulting in the first cycle residual $scCO_2$ distribution (b). Based on the residual $scCO_2$ distribution, regions of the solid surface adjacent to $scCO_2$ clusters (≤5 voxels distance) were identified and modified to become CO_2-wetting surfaces (c) for the subsequent drainage-imbibition cycles.

Armstrong, 2020; Sun, McClure, Mostaghimi, Herring, Meisenheimer, et al., 2020; Sun et al., 2019). This analysis was performed on a subsection of each data volume equivalent to a cube of 700^3 voxels from the vertical center of the full data volume, and only for residual ganglia for which the Euler characteristic, χ, is equivalent to 1. This method is based on the Gauss-Bonnet theorem, which links the topology of an object to its total curvature; for an object with known topology (i.e., $\chi = 1$), the value of total curvature (equivalent to the sum of the Gaussian curvature of the object surface and the geodesic curvature along the contact line) can be analytically determined. The Gaussian curvatures of the ganglion-fluid and ganglion-solid surfaces are measured from the imaged data, and the deficit between the analytic and measured values, termed the deficit curvature, is equivalent to the sum of the geodesic curvatures along the contact line. The deficit curvature value thus represents a macroscopic contact angle for each ganglion (e.g., rather than an average of a series values measured at discrete points along the contact line) and is less susceptible to pixelation effects at the three-phase line. In addition, this method is not biased by the number of interface points: ganglia with low and high numbers of interface points are all weighted equally.

2.4. Lattice-Boltzmann Simulation

We simulated wettability alteration during drainage-imbibition cycles using the LB method. The LB method is a numerical method for solving the Navier-Stokes equations (Chen & Doolen, 1998; Succi, 2001); here, we used a multi-relaxation time color LB model described by McClure et al. (2014). The validation of this LB implementation has confirmed that computed static and dynamic contact angles are consistent with existing slip models, and interfacial and contact line dynamics can be accurately recovered (McClure et al., 2016).

Three consecutive drainage-imbibition cycles with fluid-solid LB relaxation properties approximating $scCO_2$ and 1.0 M KI brine (see Table 1) were simulated in a 500^3 voxels subsection of the Bentheimer sandstone "dry" data volume, starting with an initial universal solid contact angle of 55° (i.e., similar to the contact angle of 54° previously reported for air-KI brine in Benteheimer Sun, McClure, Mostaghimi, Herring, Berg, Armstrong, 2020). Two significant deviations from experimental conditions were implemented: to preserve stability of the LB model, the viscosity ratio ($\mu_{scCO_2}/\mu_{\mathrm{brine}}$) was set to a value 4 × larger than the experimental value; and to ensure timely convergence of the simulated flow processes, the flow rate was set to an increased value such that the capillary number of the imbibition process was an order of magnitude larger than the experimental condition. Impacts of these deviations are discussed in Section 3.5.

The transition to a "patchy" mixed-wet state was approximated by a step-wise contact angle alteration (Figure 2). First, the drainage and imbibition stages were completed under the criteria and settings described above. At the residual state, any regions of solid surface within 5 voxels distance to $scCO_2$ phase was relabeled as weakly $scCO_2$-wet (contact angle of 125°, indicated in blue in Figure 2c). Starting from this residual end point fluid distribution and with the modified mixed-wet surface condition, the second drainage-imbibition process was simulated (again as described above). At the second residual state, the contact angle modification procedure was repeated again (preserving the $scCO_2$-wetting labels from the first residual state); and the third and final drainage-imbibition process was simulated.

3. Results and Discussion

We first present experimental results in terms of core volume-averaged measurements (Section 3.1), pore-scale fluid occupancy (Section 3.2), ganglia geometry and topology (Section 3.3), and macroscopic contact angles (Section 3.4). Then, we will compare these trends to the LB simulations (Section 3.5). Finally, we discuss these results in the context of the previously described wettability alteration mechanisms (Section 3.6) and compare to results of previous studies (Section 3.7).

3.1. Core-Averaged Experimental Results

Experimentally measured pressure curves and the trapping curve for all drainage ($scCO_2$ injection) and imbibition (brine injection) flows are shown in Figure 3.

Pressure is elevated for the first $scCO_2$ injection and gradually reduces for all subsequent injections; in contrast, the pressure increases as cycle number increases for brine injections. Pressure in the experimental system is recorded at the transducer in the injection pump, and is, therefore, an absolute value representing the pressure drop throughout all flow lines, valves, and the core.

Initial (post-$scCO_2$ injection) vs. residual (post-brine injection) saturation values are shown on the conventional trapping curve format in Figure 3 along with a standard trapping curve using Land model coefficients (c) equal to 2.5 and 5 for illustration (compare to the value of 2.52 reported by Øren et al., 2019). As anticipated, the experimental results do not conform to smooth trapping curves exemplified by the Land model (Land, 1968); indicating deviance from conventional multiphase trapping theory.

3.2. Experimental Flow Patterns and Fluid Occupancy

Visualization of the central vertical cross-section of the sample after all $scCO_2$ injections ("initial" states) and all brine injections ("residual" states) demonstrate the evolution of pore-scale $scCO_2$ occupancy (Figure 4). Initial $scCO_2$ ganglia are well distributed throughout the core (albeit at varying total saturation); in contrast, residual $scCO_2$ ganglia are essentially nonexistent in the first cycle; radially biased away from the center of the core in the second cycle, and gradually start to trap in central regions during the third and fourth cycles. This distribution is potentially due to the relatively high flow rate combined with the geometry of the core and core holder apparatus (i.e., zero wall flow, leading to higher levels of brine flushing in the central region of the core.).

Residual saturation after the first cycle is approximately 0%; we attribute this to the relatively high flow rate of imbibition ($\log Ca = -5.3$). The low residual saturation is similar to the results of Herring et al. (2016), who also showed $S_{R,1}$ near 0% for the first cycle (for experiments conducted at similar capillary number), and Dalton et al. (2020) who observed $S_{R,1}$ of approximately 6% (capillary number unreported). The low residual $scCO_2$ saturation values are in-line with recent experiments that have shown that desaturation (mobilization) for a well-connected initial phase (such as is the case in this experiment) occurs at capillary number an order of magnitude lower relative to the progressive desaturation of a disconnected fluid phase (Hu et al., 2020). We note that dissolution is possible, but unlikely, given the fluid mixing protocol and pressure-temperature uniformity of the experimental apparatus.

Pore network representations of the dry and $scCO_2$-occupied pore spaces were extracted using persistent-homology-based labeling via Diamorse for $1{,}500^3$ voxels cubed subsections of the full data. The extracted networks (Figure 5) show that $scCO_2$ tends to occupy smaller pore bodies and smaller pore throats as cycling progresses. Occupancy is expected to shift to smaller regions for higher $scCO_2$ saturation as $scCO_2$ invades

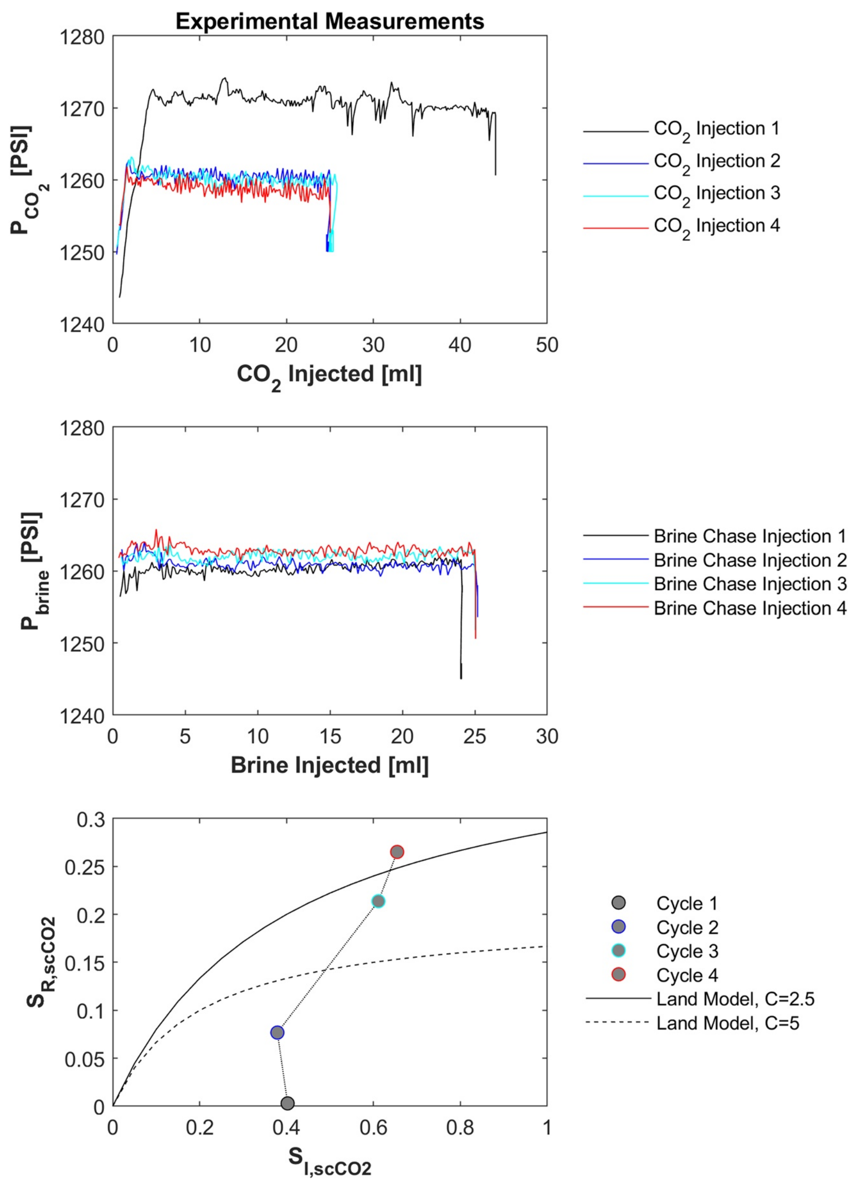

Figure 3. Experimentally measured pressure profiles during $scCO_2$ (top row) and brine (middle row) injections, and $scCO_2$ saturations for all stages as presented on the trapping curve (bottom row).

into regions with higher capillary pressure thresholds; we do observe occupancy shifts to smaller regions, however, we observe that interface mean curvature (a measure of capillary pressure) actually decreases as cycle's progress. This will be further presented and discussed in the next section.

3.3. Geometric and Topological Ganglia Characterization

Residual $scCO_2$ ganglia size distributions over cycles two-four are shown in Figure 6. As cycle number increases, the total number ganglia increases. There are relatively large ganglia present after cycle two, the size distribution shift toward smaller ganglia in cycle three, and do not change thereafter.

Topology of the $scCO_2$ phase was investigated via persistent homology, and the persistence diagrams of β_1 features (redundant connections, or loops) are shown in Figure 7. For full interpretation of persistence diagrams, the reader is referred to previous work (Herring et al., 2019; Robins et al., 2015); the key features are highlighted here. As cycling progresses, the number of loops formed by $scCO_2$ increases; this occurs for

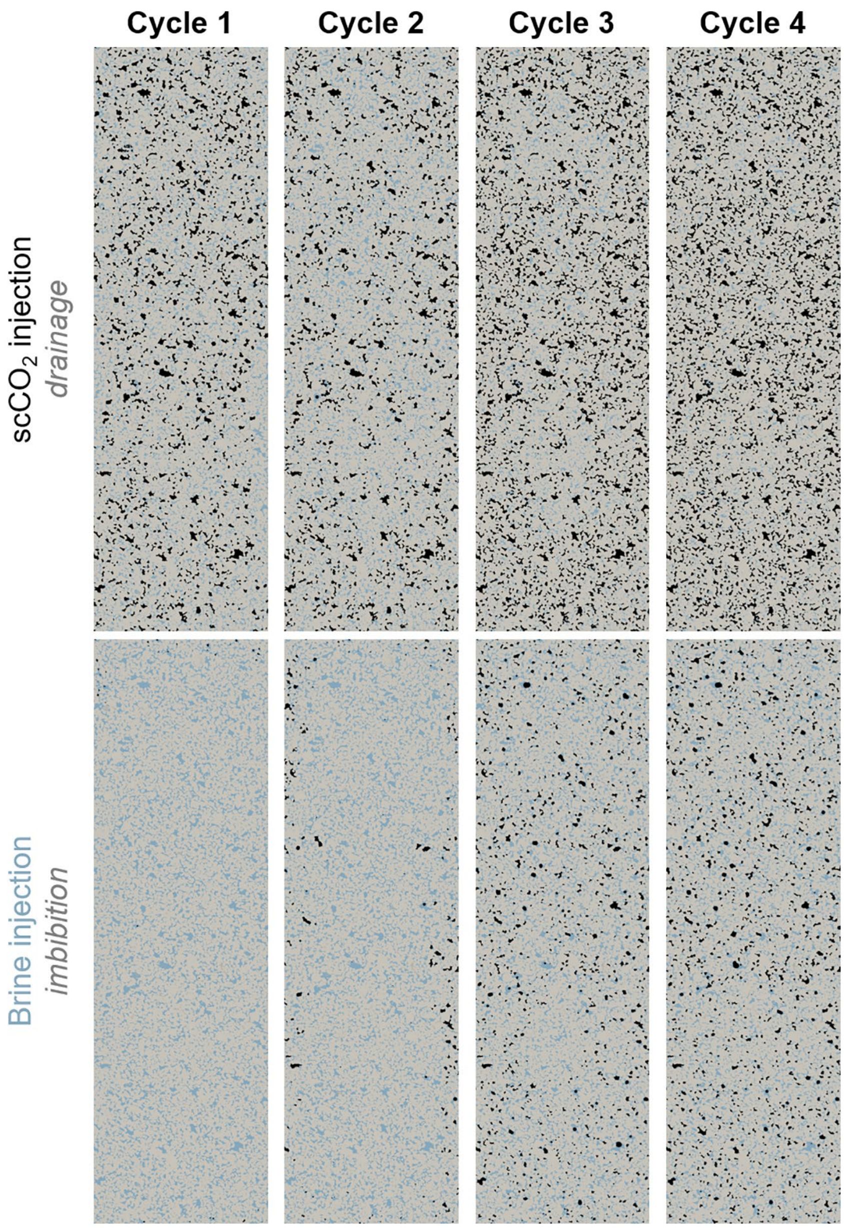

Figure 4. Top row: 2D vertical cross-sections of the Bentheimer sample at the end of $scCO_2$ injection processes; bottom row: cross-sections at the end of chase brine injections. Different phases are color-labeled: $scCO_2$ in black, brine in teal, and solid sandstone grains and clays in gray.

both S_I and S_R states. As cycles progress, the β_1 birth value distributions shift closer to 0, indicating that the thinnest sections of each loop (i.e., the smallest throat that the loop is formed through) shift to smaller radii. The death value distributions (measuring to the radius of the obstacle each loop encompasses) also shift closer to 0, indicating that the loops are contracting. These observations complement the network statistics analysis presented above; both analyses show that $scCO_2$ invades smaller pore spaces as cycling progresses; the persistent homology analysis provides additional information on the number and span of loop structures formed by $scCO_2$ phase.

Additional averaged volumetric and geometric characterization of the residual $scCO_2$ in experiments are shown in Figure 8. Residual saturation and trapping efficiency (residual saturation normalized by the previous initial saturation, S_R/S_I) increase with cycle number. Average CO_2-brine interface means curvature decreases with cycle number, indicating that capillary trapped $scCO_2$ bubbles exist at lower capillary

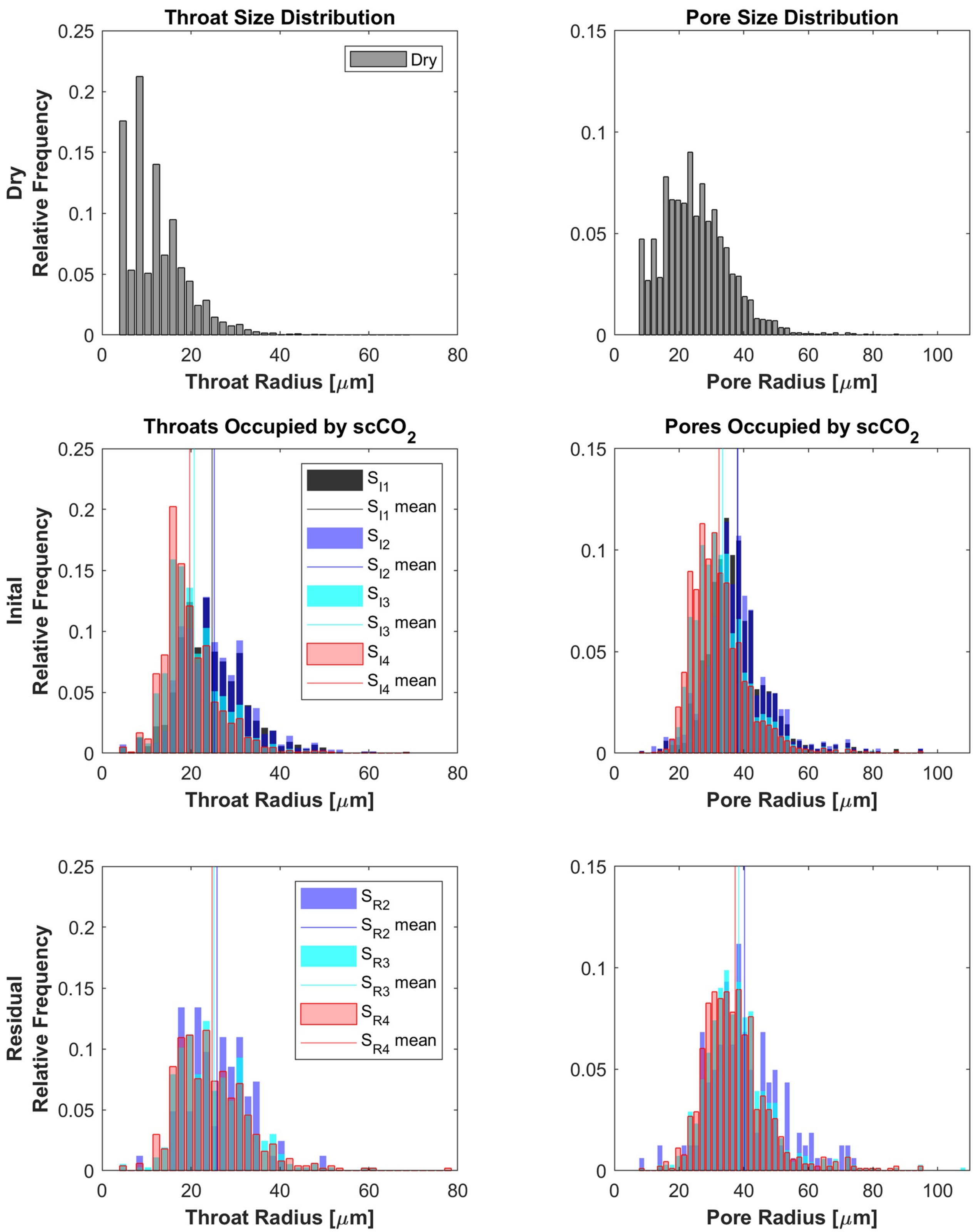

Figure 5. Pore space characteristics of the dry sandstone sample (top row) and the spaces occupied by $scCO_2$ after drainage (*middle row) and imbibition (bottom row) measured from experimental tomographic images.

10.1029/2021WR030891

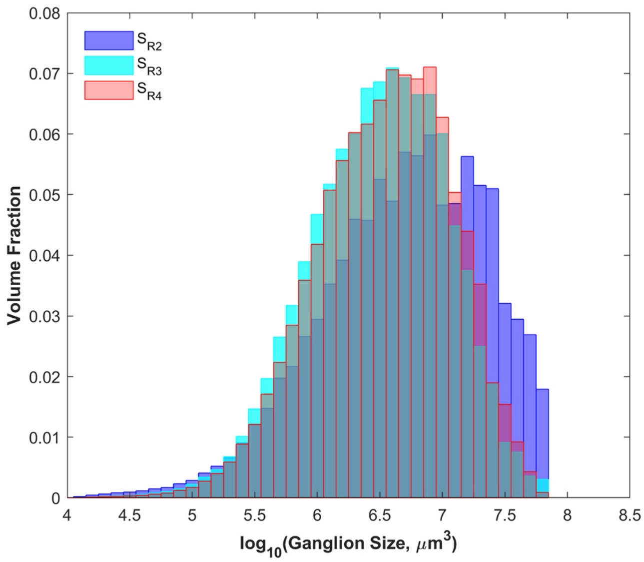

Figure 6. Histograms of residual ganglia size for cycles two through four measured from experimental tomographic images.

pressure (on average); while the apparent fraction of $scCO_2$ surface area that is comprised of the interfacial area between rock and $scCO_2$ increases (wettability-altered samples exhibit increases in rock-$scCO_2$ interfacial area as per Garfi et al., 2020). Values for the first cycle residual $scCO_2$ ganglia are not included, because the low saturation (≈0.0%) predicates that these values are dominated by only very small features assumed to be nonrepresentative.

Again, we highlight that $scCO_2$ invades smaller pore spaces (as quantified by network-based phase occupancy, and also the persistent homology topological analysis) even while interface mean curvature (proxy for capillary pressure) decreases for residual ganglia. Inspection of the full experimental series highlights that (somewhat counter-intuitively) $scCO_2$ phase connectivity and trapping both increases as the experiment progresses, supporting the results of previous experiments (Herring et al., 2016).

3.4. Macroscopic Contact Angle and Gaussian Curvature of Ganglia Interfaces

The per-ganglia distribution of macroscopic contact angles (θ^{macro}) measured on residual data subsets is shown in Figure 9; only topologically simple ganglia ($\chi = 1$) for cycles two through four were included in this analysis (there were insufficient residual ganglia present in the first cycle). The contact angle distributions shift to a less water-wet state (larger θ^{macro}) as cycle number increases: the peak of the distributions of macroscopic contact angle value increases by approximately 15° from cycle two to cycle four. In addition, numerous instances of ganglia residing at $scCO_2$-wet contact angles ($> 90^o$) are observed during cycles three and four.

The macroscopic contact angle analysis clearly indicates that the wettability of the sandstone surface evolves toward a mixed-wet state with higher contact angles as the experiment progresses.

3.5. Lattice-Boltzmann Simulation

The LB simulation was conducted on a smaller subset of data with some significant deviations from experimental conditions, as described in Section 2.4. However, the simulations do reproduce some trends observed in experiments. Pressure curves and the trapping curve for all simulated drainage ($scCO_2$ injection) and imbibition (brine injection) flows are shown in Figure 10 (compare to Figure 3). The LB-simulated pressure profiles follow the same trends with cycle numbers as the experimental pressure measurements; that is, for consecutive drainage processes $scCO_2$ pressure decreases, while for consecutive imbibition processes brine pressure increases. We note that the experimental measurements are absolute values and represent the pressure drop through the entire experimental apparatus, whereas the pressure measured in the LB simulation is a differential measurement between the inlet and outlet of the subsample, only across the 500 voxel simulation domain.

Also similarly to the experimental data, the $scCO_2$ saturation values measured from LB simulation endpoints do not produce a classic trapping model curve as shown in Figure 10; but neither does the LB simulation reproduce the experimentally observed $scCO_2$ saturations. The relatively high initial $scCO_2$ saturations achieved during LB drainage simulations are likely due to the high viscosity ratio used in LB simulations ($10 \times$ larger than that in experiments, see Table 1), and the residual saturation values are potentially suppressed due to the high imbibition capillary number of simulations an order of magnitude larger than that calculated for experiments, see Table 1. In addition, we suspect that the wettability alteration applied in simulations over-estimates the coverage and magnitude of wettability alteration manifest in experiments.

We also measured the average geometric characteristics of the residual $scCO_2$ ganglia (Figure 11). Again, the saturation trends do not follow the trends observed in experiments; however, the trends in interface mean curvature and $scCO_2$-solid interfacial area agree. The exact values of these parameters are not reproduced

10.1029/2021WR030891

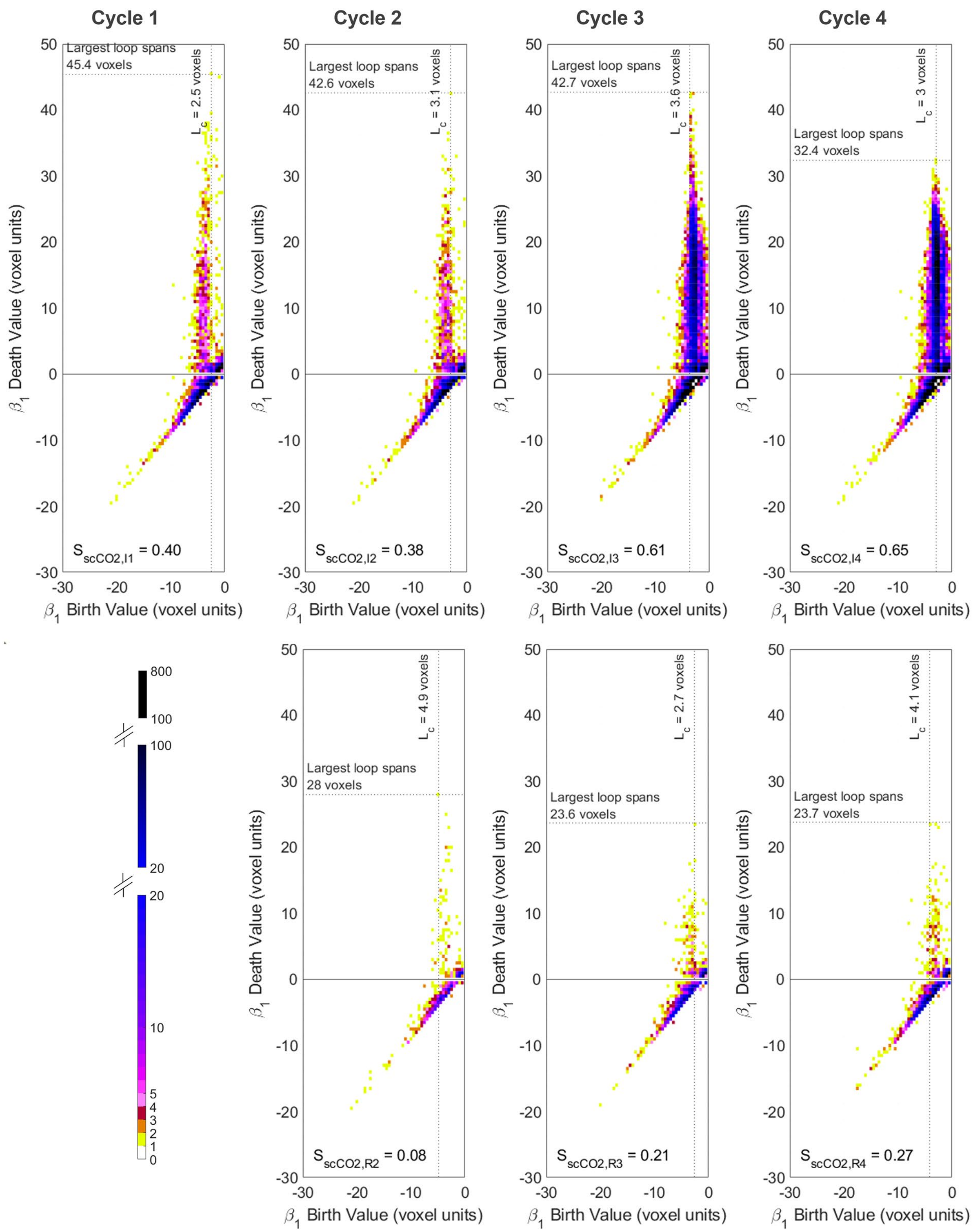

Figure 7. Persistence diagrams of β_1 features created by $scCO_2$ ganglia in the initial (top row) and residual (bottom row) scans. The first residual scan, S_{scCO_2}, $R1$ is omitted due to insufficient presence of $scCO_2$.

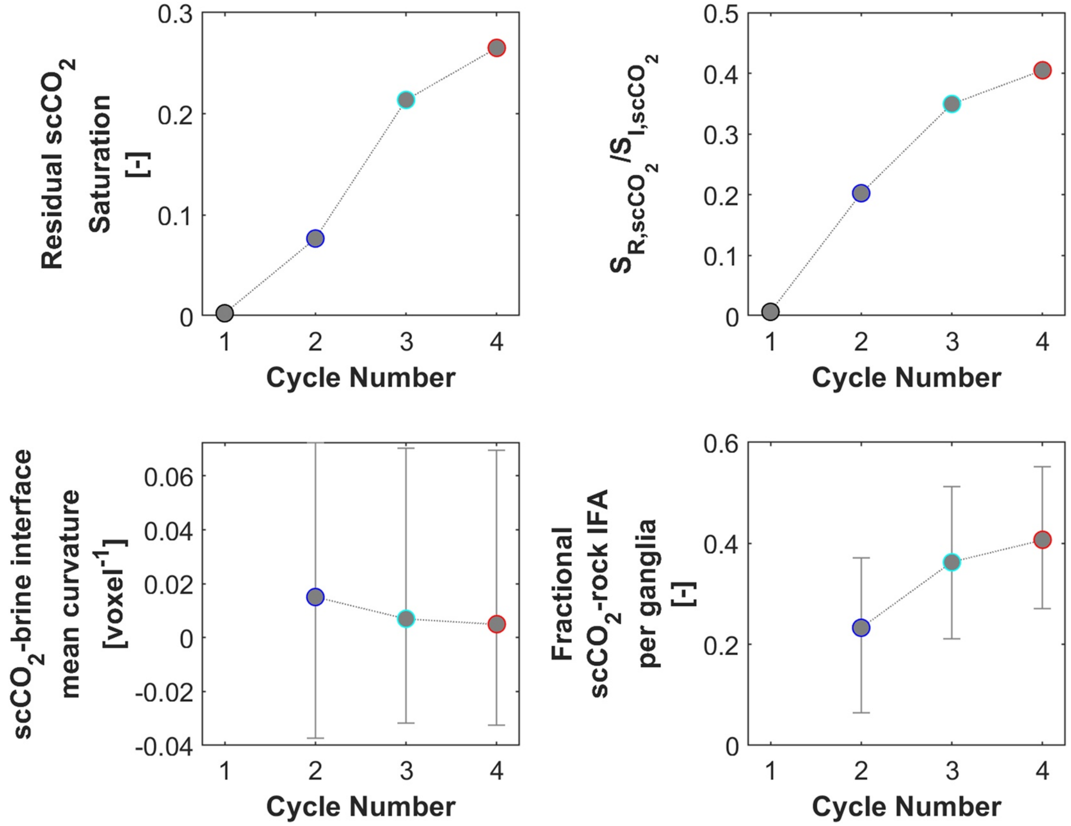

Figure 8. Volumetric and geometric characteristics of residual $scCO_2$ ganglia over multiple injection cycles measured from experimental tomographic images. Data points represent mean values; for quantities that exist on a distribution, bars represent the range between the first and third quartiles.

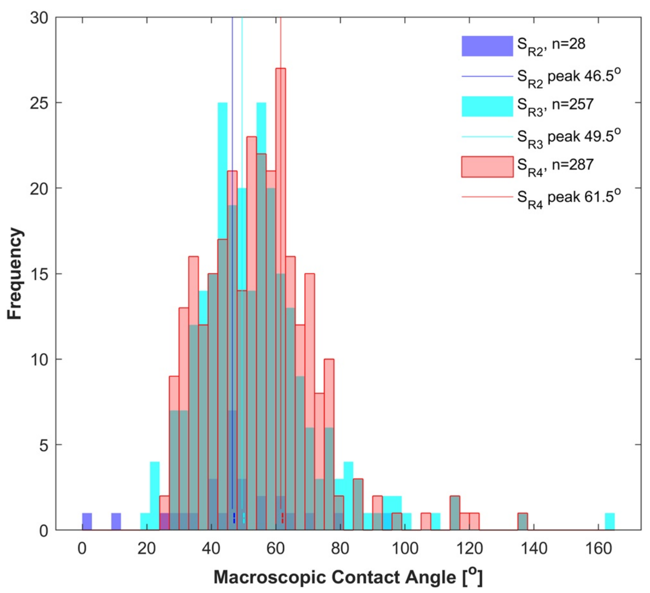

Figure 9. Macroscopic (per ganglion) contact angles (measured on experimental residual data subsections for cycles 2, 3, and 4). The distributions shift to higher mean contact angle as cycle number increases, with some ganglia exhibiting $scCO_2$-wet behavior for cycles 3 and 4.

between experiment and LB simulation (likely due to the discrepancies between experiment and simulation mentioned above), but the similarity in trends indicates that the surface modification modeled in LB simulation could produce the changes in ganglion characteristics observed in experiments.

In general, the size of residual ganglia observed in experiments tend to be much larger than those measured in LB simulation results (LB size distributions included in the Supporting Information S1); this is potentially an impact of the higher capillary number used in LB simulations (higher capillary number is correlated with smaller residual ganglia, e.g., Chatzis et al., 1988).

3.6. Wettability Alteration Mechanisms

The wettability alteration mechanisms mentioned in Section 1 occur on length scales much smaller than the resolution of the image data presented here, so we are unable to provide direct evidence of either mechanism. We have conducted additional mineralogical analyses (details in the Supporting Information S1) that provide some additional, albeit limited, insight into the potential cause of wettability transition.

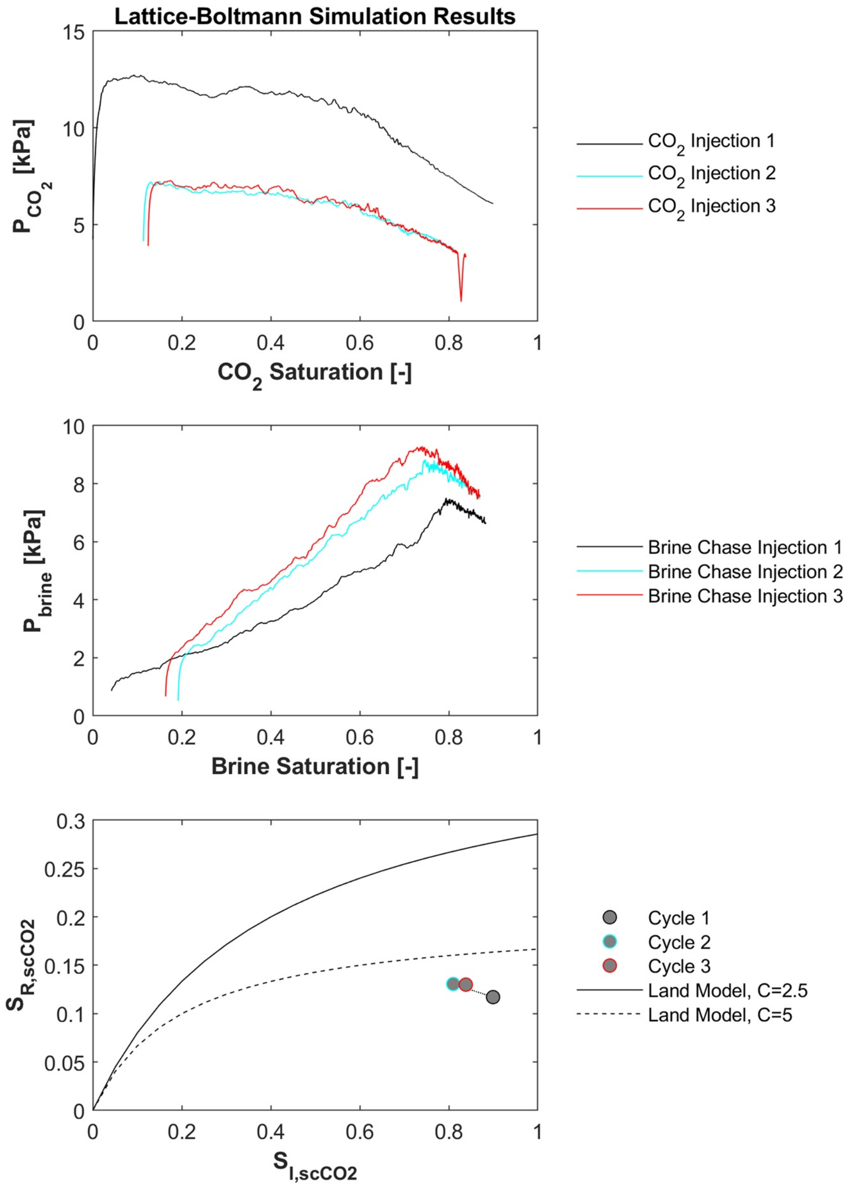

Figure 10. Pressure profiles during simulated $scCO_2$ (top row) and brine (middle row) injections, and $scCO_2$ saturations for all stages as presented on the trapping curve (bottom row).

3.6.1. Fines Migration

The Bentheimer sandstone samples investigated here are relatively clean sandstones comprised of approximately 95% quartz, with only small amounts of mineral phases susceptible to surface alteration or fines migration. Mineralogical EDX-BSE analysis conducted on an "unaltered" core and a sister core exposed to multiple cycles of $scCO_2$ and brine did not show significant differences in clay presence or morphology (mineralogical analysis presented in Supporting Information S1). Additionally, we do not observe injection pressure behavior representative of decreased permeability due to formation damage (i.e., while brine pressure slightly increases with cycle number, $scCO_2$ injection pressure decreases with cycle number). Thus, we do not find significant evidence that the observed transition to a "patchy" mixed-wet state can be attributed to fines migration or formation damage in this specific $scCO_2$-1.0 M KI brine-Bentheimer system, under these state conditions.

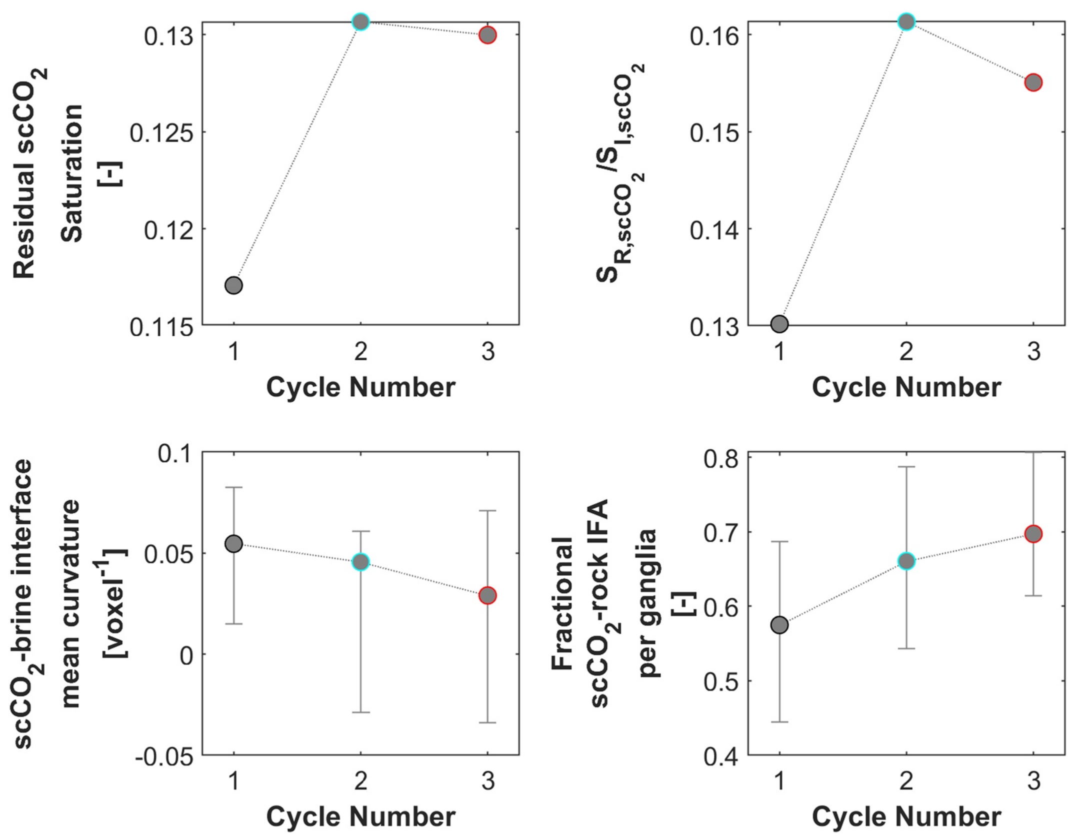

Figure 11. Volumetric and geometric characteristics of residual $scCO_2$ ganglia over multiple injection cycles measured from lattice-Boltzmann (LB) simulations. Data points represent mean values; for quantities that exist on a distribution, bars represent the range between the first and third quartiles.

3.6.2. $scCO_2$ Adhesion

While $scCO_2$ adhesion to surfaces has been previously observed, the mechanism is not fully understood. Assuming that the impact of adhesion can be approximated by a transition to $scCO_2$-wet contact angles on solid surfaces near $scCO_2$ ganglia, the LB simulations investigated in this study approximate a system impacted by $scCO_2$ adhesion. The wettability modification scheme applied in our LB simulations likely over-estimates the magnitude and coverage of contact angle change. Even so, the simulation results (in terms of pressure curves, mean curvature, and fractional $scCO_2$-rock interfacial area) exhibit the same trends as the experimental results. The exact values of these parameters are not reproduced between experiment and LB simulation (likely due to the discrepancies in viscosity and capillary number between experiment and simulation, and potentially over-application of contact angle increase and coverage), but the trends for these measurements show good agreement, indicating that the surface modification modeled in LB simulation could produce the changes in ganglion characteristics observed in experiments. Refinement of model parameters and wettability modification could improve the comparison.

3.7. Comparison With Previous Studies

The results presented here support previous studies reporting increased residual trapping over cyclic $scCO_2$-brine injections, but there are some discrepancies. For example, Abdoulghafour et al. (2020), Herring et al. (2016), and Herring, Wildenschild, et al. (2018) reported that the size distribution of ganglia shifted to larger volumes as cycle number increased, whereas the Bentheimer cores of Dalton et al. (2020) do not show changes in ganglia size distribution; and the results presented here show a decrease in ganglia size from the second cycle to the third and insignificant changes in ganglia size distribution thereafter. The cores used in experiments in Herring et al. (2016) and those investigated here are sister cores from the same larger block of Bentheimer sandstone, and significant differences in mineral composition or distribution are not expected. Rather, we suggest that the difference in observed ganglia size is potentially due to differences in experimental set-up; for example, Herring et al. (2016) and Herring, Wildenschild, et al. (2018) used a "porous plate" configuration (i.e., semipermeable hydrophilic membrane placed at the base of the core, brine was withdrawn or injected from the bottom of the core while $scCO_2$ was held at constant pressure and allowed to enter/leave the core via the upper endcap), while Dalton et al. (2020) and the current experimental set-up both use "coinjection" core holders (i.e., injection ports for both fluids at the bottom of the core and a combined effluent line exiting at the top of the core). The difference in configuration leads to different (absolute) pressure behavior, that is, for drainage in a porous plate set-up the brine pressure is decreased while $scCO_2$ pressure is held constant (and so pore pressure is always $\leq P_{scCO2} = 8.6$ MPa/1,250 PSI), whereas for a coinjection system the $scCO_2$ and brine pressures (and correspondingly, total pore pressure) are increased during both drainage and imbibition (i.e., pore pressure always ≥8.6 MPa/1,250 PSI in the current experiment). Both experimental systems eventuate shifts in capillary pressure, but to different extent; this could cause differences in the pore spaces exposed to $scCO_2$ adhesion and result in slightly different ganglia characteristics and level of residual trapping between experiment types.

Ge et al. (2022) reported that fines migration (induced via original saturation with CO_2-saturated water) increased residual saturation of $scCO_2$ relative to core flooding experiments where fines migration is unlikely to occur (i.e., cores originally saturated with water not equilibrated with $scCO_2$); the authors of that study attributed the elevated trapping to pore throat blockage by fines. We note that the original saturating fluid (unsaturated vs. saturated with $scCO_2$) would also likely impact whether adhesion might occur. While we did not directly observe evidence of pore throat blockage in this experiment, higher-resolution imaging might further elucidate this issue.

Adhesion is likely to be highly dependent on aqueous chemistry parameters; this indicates that experiments conducted under different state conditions or with different aqueous compositions (e.g., Garing & Benson, 2019; Ruprecht et al., 2014; Saeedi & Rezaee, 2012) may not exhibit adhesion nor associated changes in capillary pressure, or residual trapping and evolution of ganglia characteristics. If adhesion is pressure-sensitive, as indicated by Dickson et al. (2006), then depressurization and vacuum treatment of cores prior to flow experiments (e.g., as was conducted in the experiments of Garing & Benson, 2019) might reverse the adhesion and return the rock surface to an unaltered state.

Another difference between the study of Ruprecht et al. (2014) and the current study is that the former study utilized fired cores, intended to prevent clays from swelling with fluids. While we did not observe changes in clay presence or morphology due to cycling, it is possible that the firing of cores (particularly for different sandstones) might result in significantly different starting surface conditions leading to different behavior in the two experimental systems. The study of Garing and Benson (2019) demonstrated that firing does not have an impact on the measured capillary pressure-saturation relationship for primary drainage of $scCO_2$ in Berea sandstone; however, note that water (not brine) was used as the wetting fluid in those experiments and the impact of flow processes beyond primary drainage was not investigated.

Previous studies have shown that residual trapping is significantly reduced in mixed-wet media, compared to uniformly water-wet conditions (Alhammadi et al., 2017; Al-Menhali & Krevor, 2016; Al-Menhali et al., 2016; Blunt, 1998; Singh et al., 2016). In these previous studies, enhanced mobility of the non-aqueous phase was attributed to connective layers enabled by the mixed-wetting pattern of the media. We do not observe connected $scCO_2$ layers in our experimental results, indicating that the CO_2-wet regions in this system are sufficiently disconnected so as to prevent the formation of connected pathways, that is, the system observed here has a "patchy" mixed-wettability state where the $scCO_2$-wet regions are discontinuous.

4. Conclusions

We have presented X-ray tomography image-based results from an experiment of four drainage-imbibition cycles with $scCO_2$ and brine in Bentheimer sandstone, and demonstrated that measured pressure shifted and residual trapping increased with cycle number. $ScCO_2$ ganglia characteristics (surface areas, fluid-fluid mean and Gaussian curvatures, topological measures) also progressively changed with cycle number. Network and persistent homology analysis showed that $scCO_2$ ganglia occupied smaller pore throats and bodies, and formed increasing numbers of loops as cycling progressed; even as interface mean curvature decreased. Deficit curvature analysis indicated a shift in macroscopic contact angle distributions over the course of the four cycles, with histogram peaks increasing by ∼15° from cycle two to cycle four.

The quantitative experimental measurements indicate that this $scCO_2$-brine-Bentheimer sandstone system undergoes a transition to a mixed-wet state over the course of four drainage-imbibition cycles. However, in contrast to some other experimental work where mixed-wet media exhibit a reduction in residual trapping, this system shows significant increases in residual trapping. LB simulations approximating a transition in wettability to a "patchy" mixed-wet state where the CO_2-wet regions are discontinuous produce similar trends in geometric properties of residual $scCO_2$ ganglia compared to experimental results. Thus, we propose that the results of the experiments presented here indicate a transition to a patchy mixed-wet state that results in increased residual trapping of $scCO_2$.

We cannot directly determine the cause of wettability alteration from these experiments. We did not observe significant evidence of fines migration or formation damage in this study. The LB simulation results indicate that it is possible that CO_2 adhesion in regions local to residual $scCO_2$ ganglia could produce the results observed here. Both of these mechanisms are likely to be impacted by state conditions and brine composition, as well as the presence of other minerals, especially if fines are present and are mobilized. Parametric studies incorporating characterization of both of these surfaces chemistry processes should be a priority in future experiments.

If the wettability alteration observed herein is indeed representative of geologic reservoir responses, safe and effective storage of $scCO_2$ via residual trapping may play a larger role than current estimates suggest. Furthermore, if the mechanism(s) underlying the observed wettability alteration can be fully pinned-down, there is potential that injection conditions could be manipulated in engineered sequestration operations to deliberately increase residual trapping.

Data Availability Statement

Imaged data were scanned at the "National Laboratory for X-ray Micro Computed Tomography (CTLab)" based at the Australian National University (ANU) using a HeliScan MicroCT system. Segmented 3D volumes are publically available via the ANU data commons at https://datacommons.anu.edu.au/DataCommons/item/anudc:6119 (DOI: https://dx.doi.org/10.25911/6181fc5c9b8ed).

Acknowledgments
A. Herring acknowledges financial support via Australian Research Council (ARC) DE180100082 and the ANU/UNSW Digicore Research Consortium, and A. Herring and M. Saadatfar both acknowledge financial support from ARC IC180100008. C. Sun acknowledges the financial support by the National Natural Science Foundation of China (No. 42102149) and the Fundamental Research Funds for the Central Universities (No. 2462021BJRC004).

References

Abdoulghafour, H., Sarmadivaleh, M., Hauge, L. P., Fernø, M., & Iglauer, S. (2020). Capillary pressure characteristics of CO_2-brine-sandstone systems. *International Journal of Greenhouse Gas Control*, *94*, 102876. https://doi.org/10.1016/j.ijggc.2019.102876

Abidoye, L. K., Khudaida, K. J., & Das, D. B. (2015). Geological carbon sequestration in the context of two-phase flow in porous media: A review. *Critical Reviews in Environmental Science and Technology*, *45*(11), 1105–1147. https://doi.org/10.1080/10643389.2014.924184

Adeoye, J. T., Menefee, A. H., Xiong, W., Wells, R. K., Skemer, P., Giammar, D. E., & Ellis, B. R. (2017). Effect of transport limitations and fluid properties on reaction products in fractures of unaltered and serpentinized basalt exposed to high PCO_2 fluids. *International Journal of Greenhouse Gas Control*, *63*, 310–320. https://doi.org/10.1016/J.IJGGC.2017.06.003

Akbarabadi, M., & Piri, M. (2013). Relative permeability hysteresis and capillary trapping characteristics of supercritical CO_2/brine systems: An experimental study at reservoir conditions. *Advances in Water Resources*, *52*, 190–206. https://doi.org/10.1016/j.advwatres.2012.06.014

Akbarabadi, M., & Piri, M. (2015). Co-sequestration of SO_2 with supercritical CO_2 in carbonates: An experimental study of capillary trapping, relative permeability, and capillary pressure. *Advances in Water Resources*, *77*, 44–56. https://doi.org/10.1016/j.advwatres.2014.08.011

Alhammadi, A. M., Alratrout, A., Singh, K., Bijeljic, B., & Blunt, M. J. (2017). In situ characterization of mixed-wettability in a reservoir rock at subsurface conditions. *Scientific Reports*, *7*(1). https://doi.org/10.1038/s41598-017-10992-w

Al-Menhali, A. S., & Krevor, S. C. (2016). Capillary trapping of CO_2 in oil reservoirs: Observations in a mixed-wet carbonate rock. *Environmental Science & Technology*, *50*(5), 2727–2734. https://doi.org/10.1021/acs.est.5b05925

Al-Menhali, A. S., Menke, H. P., Blunt, M. J., & Krevor, S. C. (2016). Pore scale observations of trapped CO_2 in mixed-wet carbonate rock: Applications to storage in oil fields. *Environmental Science and Technology*, *50*(18), 10282–10290. https://doi.org/10.1021/acs.est.6b03111

Andersson, L., Herring, A. L., Schlueter, S., & Wildenshild, D. (2018). Defining a novel pore-body to pore-throat "Morphological Aspect Ratio" that scales with residual non-wetting phase capillary trapping in porous media. *Advances in Water Resources*, *122*, 251–262. https://doi.org/10.1016/j.advwatres.2018.10.009

Andrew, M., Menke, H., Blunt, M. J., & Bijeljic, B. (2015). The imaging of dynamic multiphase fluid flow using synchrotron-based X-ray microtomography at reservoir conditions. *Transport in Porous Media*, *110*(1), 1–24. https://doi.org/10.1007/s11242-015-0553-2

Bachu, S. (2003). Screening and ranking of sedimentary basins for sequestration of CO_2 in geological media in response to climate change. *Environmental Geology*, *44*(3), 277–289. https://doi.org/10.1007/s00254-003-0762-9

Bachu, S. (2015). Review of CO_2 storage efficiency in deep saline aquifers. *International Journal of Greenhouse Gas Control*, *40*, 188–202. https://doi.org/10.1016/j.ijggc.2015.01.007

Bachu, S., & Bennion, B. (2008). Effects of in situ conditions on relative permeability characteristics of CO_2-brine systems. *Environmental Geology*, *54*(8), 1707–1722. https://doi.org/10.1007/s00254-007-0946-9

Bachu, S., Bennion, D. B., Clark, K., Nw, R., & Tn, A. (2009). *Interfacial tension between CO_2, freshwater, and brine in the range of pressure from (2 to 27) MPa, temperature from (20 to 125)°C, and water salinity from (0 to 334,000) mg·L^{-1}* (pp. 765–775). https://doi.org/10.1021/je800529x

Bennion, D. B., & Bachu, S. (2013). The impact of interfacial tension and pore size distribution/capillary pressure character on CO_2 relative permeability at reservoir conditions in CO_2-brine systems. In *SPE/DOE symposium on improved oil recovery*. Society of Petroleum Engineers. https://doi.org/10.2118/99325-MS

Blunt, M. J. (1998). Physically-based network modeling of multiphase flow in intermediate-wet porous media. *Journal of Petroleum Science and Engineering*, *20*(3–4), 117–125. https://doi.org/10.1016/S0920-4105(98)00010-2

Boot-Handford, M. E., Abanades, J. C., Anthony, E. J., Blunt, M. J., Brandani, S., Mac Dowell, N., et al. (2014). Carbon capture and storage update. *Energy & Environmental Science*, *7*(1). https://doi.org/10.1039/c3ee42350f

Bui, M., Adjiman, C. S., Bardow, A., Anthony, E. J., Boston, A., Brown, S., et al. (2018). Carbon capture and storage (CCS): The way forward. *Energy & Environmental Science*, *11*(5). https://doi.org/10.1039/c7ee02342a

Burnside, N. M., & Naylor, M. (2014). Review and implications of relative permeability of CO_2/brine systems and residual trapping of CO_2. *International Journal of Greenhouse Gas Control*, *23*, 1–11. https://doi.org/10.1016/j.ijggc.2014.01.013

Chatzis, I., Kuntamukkula, M. S., & Morrow, N. R. (1988). Effect of capillary number on the microstructure of residual oil in strongly water-wet sandstones. *SPE Reservoir Engineering*, *3*(3), 902–912. https://doi.org/10.2118/13213-pa

Chen, S., & Doolen, G. D. (1998). Lattice Boltzmann method for fluid flows. *Annual Review of Fluid Mechanics*, *30*(1), 329–364. https://doi.org/10.1146/annurev.fluid.30.1.329

Chiquet, P., Broseta, D., & Thibeau, S. (2007). Wettability alteration of caprock minerals by carbon dioxide. *Geofluids*, *7*(2), 112–122. https://doi.org/10.1111/j.1468-8123.2007.00168.x

Dalton, L. E., Crandall, D., & Goodman, A. (2020). Characterizing the evolution of trapped $scCO_2$ curvature in Bentheimer and Nugget sandstone pore geometry. *Geofluids*, *2020*, 1–11. https://doi.org/10.1155/2020/3016595

Delgado-Friedrichs, O., Robins, V., & Sheppard, A. (2015). Skeletonization and partitioning of digital images using discrete Morse theory. *IEEE Transactions on Pattern Analysis and Machine Intelligence*, *37*(3), 654–666. https://doi.org/10.1109/TPAMI.2014.2346172

Deng, W., Balhoff, M., & Cardenas, M. B. (2015). Influence of dynamic factors on nonwetting fluid snap-off in pores. *Water Resources Research*, *51*(11), 9182–9189. https://doi.org/10.1002/2015WR017261

De Silva, G. P., Ranjith, P. G., & Perera, M. S. (2015). Geochemical aspects of CO_2 sequestration in deep saline aquifers: A review. *Fuel*, *155*, 128–143. https://doi.org/10.1016/j.fuel.2015.03.045

Dickson, J. L., Gupta, G., Horozov, T. S., Binks, B. P., & Johnston, K. P. (2006). *Wetting phenomena at the CO_2/water/glass interface*. https://doi.org/10.1021/LA0527238

Edlmann, K., Hinchliffe, S., Heinemann, N., Johnson, G., Ennis-King, J., & McDermott, C. I. (2019). Cyclic CO_2–H_2O injection and residual trapping: Implications for CO_2 injection efficiency and storage security. *International Journal of Greenhouse Gas Control*, *80*, 1–9. https://doi.org/10.1016/j.ijggc.2018.11.009

El-Maghraby, R. M., & Blunt, M. J. (2013). Residual CO_2 trapping in Indiana limestone. *Environmental Science & Technology*, *47*(1), 227–233. https://doi.org/10.1021/es304166u

Fan, M., McClure, J. E., Armstrong, R. T., Shabaninejad, M., Dalton, L. E., Crandall, D., & Chen, C. (2020). Influence of clay wettability alteration on relative permeability. *Geophysical Research Letters*, *47*(18), e2020GL088545. https://doi.org/10.1029/2020GL088545

Galal, S. K., Elgibaly, A. A., & Elsayed, S. K. (2016). Formation damage due to fines migration and its remedial methods. *Egyptian Journal of Petroleum*, *25*(4), 515–524. https://doi.org/10.1016/j.ejpe.2015.11.005

Garfi, G., John, C. M., Lin, Q., Berg, S., & Krevor, S. C. (2020). Fluid surface coverage showing the controls of rock mineralogy on the wetting state. *Geophysical Research Letters*, *47*(8), e2019GL086380. https://doi.org/10.1029/2019gl086380

Garing, C., & Benson, S. M. (2019). CO_2 wettability of sandstones: Addressing conflicting capillary behaviors. *Geophysical Research Letters*, *46*(2), 776–782. https://doi.org/10.1029/2018GL081359

Ge, J., Zhang, X., & Le-Hussain, F. (2022). Fines migration and mineral reactions as a mechanism for CO_2 residual trapping during CO_2 sequestration. *Energy*, *239*, 122233. https://doi.org/10.1016/J.ENERGY.2021.122233

Ge, J., Zhang, X., Othman, F., Wang, Y., Roshan, H., & Le-Hussain, F. (2020). Effect of fines migration and mineral reactions on CO_2-water drainage relative permeability. *International Journal of Greenhouse Gas Control*, *103*, 103184. https://doi.org/10.1016/j.ijggc.2020.103184

Herring, A. L., Andersson, L., Schlüter, S., Sheppard, A., & Wildenschild, D. (2015). Efficiently engineering pore-scale processes: Force balance and topology during nonwetting phase trapping in porous media. *Advances in Water Resources*, *79*, 91–102. https://doi.org/10.1016/j.advwatres.2015.02.005

Herring, A. L., Andersson, L., & Wildenschild, D. (2016). Enhancing residual trapping of supercritical CO_2 via cyclic injections. *Geophysical Research Letters*, *43*(18), 9677–9685. https://doi.org/10.1002/2016GL070304

Herring, A. L., Gilby, F. J., Li, Z., McClure, J. E., Turner, M., Veldkamp, J. P., et al. (2018). Observations of nonwetting phase snap-off during drainage. *Advances in Water Resources*, *121*, 32–43. https://doi.org/10.1016/J.ADVWATRES.2018.07.016

Herring, A. L., Harper, E. J., Andersson, L., Sheppard, A., Bay, B. K., & Wildenschild, D. (2013). Effect of fluid topology on residual nonwetting phase trapping: Implications for geologic CO_2 sequestration. *Advances in Water Resources*, *62*, 47–58. https://doi.org/10.1016/j.advwatres.2013.09.015

Herring, A. L., Middleton, J., Walsh, R., Kingston, A., & Sheppard, A. (2017). Flow rate impacts on capillary pressure and interface curvature of connected and disconnected fluid phases during multiphase flow in sandstone. *Advances in Water Resources*, *107*, 460–469. https://doi.org/10.1016/j.advwatres.2017.05.011

Herring, A. L., Robins, V., Saadatfar, M., Young, B., Knackstedt, M., & Sheppard, A. (2018). Topological persistence of heterogeneous sandstone. In *international symposium of the society of core analysts*. Trondheim, Norway. Retrieved from http://jgmaas.com/SCA/2018/SCA2018-059.pdf

Herring, A. L., Robins, V., & Sheppard, A. P. (2019). Topological persistence for relating microstructure and capillary fluid trapping in sandstones. *Water Resources Research*, *55*(1), 555–573. https://doi.org/10.1029/2018WR022780

Herring, A. L., Wildenschild, D., Andersson, L., Robins, V., & Sheppard, A. P. (2018). The impact of cyclic injection cycles on capillary trapping: Comparison of ambient and reservoir condition experiments. In *14th international conference on greenhouse gas control technologies, GHGT-14*. Melbourne, Australia.

Hu, Y., She, Y., Patmonoaji, A., Zhang, C., & Suekane, T. (2020). Effect of capillary number on morphological characterizations of trapped gas bubbles: Study by using micro-tomography. *International Journal of Heat and Mass Transfer*, *163*, 120508. https://doi.org/10.1016/J.IJHEATMASSTRANSFER.2020.120508

Huang, R., Herring, A. L., & Sheppard, A. (2021). Effect of saturation and image resolution on representative elementary volume and topological quantification: An experimental study on Bentheimer sandstone using micro-CT. *Transport in Porous Media*, *137*, 1–30. https://doi.org/10.1007/s11242-021-01571-9

IEA. (2020). *Direct air capture (Tech. Rep.)*. IEA. Retrieved from https://www.iea.org/reports/direct-air-capture

Iglauer, S. (2017). CO_2-water-rock wettability: Variability, influencing factors, and implications for CO_2 geostorage. *Accounts of Chemical Research*, *50*(5), 1134–1142. https://doi.org/10.1021/acs.accounts.6b00602

IPCC. (2005). In B. Metz, O. Davidson, H. d. Coninck, M. Loos, & L. Meyer (Eds.), *IPCC special report on carbon dioxide capture and storage*.

IPCC. (2014). *Climate change 2014: Synthesis report. Contribution of working groups I, II and III to the fifth assessment report of the intergovernmental panel on climate change (Tech. Rep.)*. Geneva, Switzerland: IPCC.

IPCC. (2019). *Global warming of 1.5°C. An IPCC special report on the impacts of global warming of 1.5°C above pre-industrial levels and related global greenhouse gas emission pathways, in the context of strengthening the global response to the threat of climate change, sustainable development, and efforts to eradicate poverty (Tech. Rep.)*.

Jones, F. O. (1964). Influence of chemical composition of water on clay blocking of permeability. *Journal of Petroleum Technology*, *16*(04), 441–446. https://doi.org/10.2118/631-pa

Jung, J.-W., & Wan, J. (2012). Supercritical CO_2 and ionic strength effects on wettability of silica surfaces: Equilibrium contact angle measurements. *Energy & Fuels*, *26*(9), 6053–6059. https://doi.org/10.1021/ef300913t

Khilar, K. C., & Fogler, H. S. (1983). Water sensitivity of sandstones. *Society of Petroleum Engineers Journal*, *23*(1), 55–64. https://doi.org/10.2118/10103-PA

Kim, Y., Wan, J., Kneafsey, T. J., & Tokunaga, T. K. (2012). Dewetting of silica surfaces upon reactions with supercritical CO_2 and brine: Pore-scale studies in micromodels. *Environmental Science & Technology*, *46*(7), 4228–4235. https://doi.org/10.1021/es204096w

Kimbrel, E. H., Herring, A. L., Armstrong, R. T., Lunati, I., Bay, B. K., & Wildenschild, D. (2015). Experimental characterization of nonwetting phase trapping and implications for geologic CO_2 sequestration. *International Journal of Greenhouse Gas Control*, *42*, 1–15. https://doi.org/10.1016/j.ijggc.2015.07.011

Krevor, S. C., Blunt, M. J., Benson, S. M., Pentland, C. H., Reynolds, C., Al-Menhali, A., & Niu, B. (2015). Capillary trapping for geologic carbon dioxide storage—From pore-scale physics to field-scale implications. *International Journal of Greenhouse Gas Control*, *40*, 221–237. https://doi.org/10.1016/j.ijggc.2015.04.006

Krevor, S. C., Pini, R., Zuo, L., & Benson, S. M. (2012). Relative permeability and trapping of CO_2 and water in sandstone rocks at reservoir conditions. *Water Resources Research*, *48*(2), 2532. https://doi.org/10.1029/2011WR010859

Land, C. (1968). Calculation of imbibition relative permeability for two-and three-phase flow from rock properties. *Old SPE Journal*, *8*(2), 149–156. https://doi.org/10.2118/1942-pa

Latham, S. J., Kingston, A. M., Recur, B., Myers, G. R., Delgado-Friedrichs, O., & Sheppard, A. P. (2018). Reprojection alignment for trajectory perturbation estimation in microtomography. *IEEE Transactions on Computational Imaging*, *4*(2), 271–283. https://doi.org/10.1109/tci.2018.2811945

Latham, S. J., Varslot, T., & Sheppard, A. (2008). Automated registration for augmenting micro-CT 3D images. *ANZIAM Journal*, *50*, C534–C548. https://doi.org/10.21914/ANZIAMJ.V50I0.1389

Li, X., Akbarabadi, M., Karpyn, Z. T., Piri, M., & Bazilevskaya, E. (2015). Experimental investigation of carbon dioxide trapping due to capillary retention in saline aquifers. *Geofluids*, *15*(4), 563–576. https://doi.org/10.1111/gfl.12127

Lu, J., Kordi, M., Hovorka, S. D., Meckel, T. A., & Christopher, C. A. (2013). Reservoir characterization and complications for trapping mechanisms at Cranfield CO_2 injection site. *International Journal of Greenhouse Gas Control*, *18*, 361–374. https://doi.org/10.1016/J.IJGGC.2012.10.007

Mahmud, W., & Nguyen, V. (2006). Effects of snap-off in imbibition in porous media with different spatial correlations. *Transport in Porous Media*, *64*(3), 279–300. https://doi.org/10.1007/s11242-005-4042-x

Mansoori, S. A., Iglauer, S., Pentland, C. H., Bijeljic, B., & Blunt, M. J. (2009). Measurements of non-wetting phase trapping applied to carbon dioxide storage. *Energy Procedia*, *1*(1), 3173–3180. https://doi.org/10.1016/j.egypro.2009.02.100

McClure, J. E., Berrill, M. A., Gray, W. G., & Miller, C. T. (2016). Tracking interface and common curve dynamics for two-fluid flow in porous media. *Journal of Fluid Mechanics*, *796*, 211–232. https://doi.org/10.1017/jfm.2016.212

McClure, J. E., Prins, J., & Miller, C. (2014). A novel heterogeneous algorithm to simulate multiphase flow in porous media on multicore CPU-GPU systems. *Computer Physics Communications*, *185*(7), 1865–1874. https://doi.org/10.1016/J.CPC.2014.03.012

McCool, B., & Tripp, C. P. (2005). Inaccessible hydroxyl groups on silica are accessible in supercritical CO_2. *Journal of Physical Chemistry*, *109*(18), 8914–8919. https://doi.org/10.1021/jp050192q

Muecke, T. W. (1979). Formation fines and factors controlling their movement in porous media. *Journal of Petroleum Technology*, *31*(2), 144–150. https://doi.org/10.2118/7007-PA

Mungan, N. (1965). Permeability reduction through changes in pH and salinity. *Journal of Petroleum Technology*, *17*(12), 1449–1453. https://doi.org/10.2118/1283-pa

Myers, G. R., Kingston, A. M., Varslot, T. K., & Sheppard, A. P. (2011). Extending reference scan drift correction to high-magnification high-cone-angle tomography. *Optics Letters*, *36*(24), 4809–4811. https://doi.org/10.1364/OL.36.004809

Nguyen, V. H., Sheppard, A. P., Knackstedt, M. A., & Val Pinczewski, W. (2006). The effect of displacement rate on imbibition relative permeability and residual saturation. *Journal of Petroleum Science and Engineering*, *52*(1–4), 54–70. https://doi.org/10.1016/j.petrol.2006.03.020

Niu, B., Al-Menhali, A., & Krevor, S. C. (2015). The impact of reservoir conditions on the residual trapping of carbon dioxide in Berea sandstone. *Water Resources Research*, *51*(4), 2009–2029. https://doi.org/10.1002/2014WR016441

Ohser, J., & Mücklich, F. (2001). *Statistical analysis of microstructures in materials science*. New York. https://doi.org/10.1046/j.1365-2389.2001.00418-9.x

Øren, P., Ruspini, L., Saadatfar, M., Sok, R., Knackstedt, M., & Herring, A. L. (2019). In situ pore-scale imaging and image-based modeling of capillary trapping for geological storage of CO_2. *International Journal of Greenhouse Gas Control*, *87*, 34–43. https://doi.org/10.1016/J.IJGGC.2019.04.017

Othman, F., Naufaliansyah, M. A., & Hussain, F. (2019). Effect of water salinity on permeability alteration during CO sequestration. *Advances in Water Resources*, *127*, 237–251. https://doi.org/10.1016/j.advwatres.2019.03.018

Peksa, A. E., Wolf, K.-H. A., Slob, E. C., Chmura, ., & Zitha, P. L. (2016). Original and pyrometamorphical altered Bentheimer sandstone; petrophysical properties, surface, and dielectric behavior. *Journal of Petroleum Science and Engineering*, *149*. https://doi.org/10.1016/j.petrol.2016.10.024

Peksa, A. E., Wolf, K.-H. A., & Zitha, P. L. (2015). Bentheimer sandstone revisited for experimental purposes. *Marine and Petroleum Geology*, *67*, 701–719. https://doi.org/10.1016/j.marpetgeo.2015.06.001

Pentland, C. H., El-Maghraby, R., Iglauer, S., & Blunt, M. J. (2011). Measurements of the capillary trapping of supercritical carbon dioxide in Berea sandstone. *Geophysical Research Letters*, *38*(6), L06401. https://doi.org/10.1029/2011GL046683

Pentland, C. H., Itsekiri, E., Al-Mansoori, S., Iglauer, S., Bijeljic, B., & Blunt, M. (2010). Measurement of nonwetting-phase trapping in sandpacks. *SPE Journal*, *15*(2), 274–281. https://doi.org/10.2118/115697-pa

Plug, W. J., & Bruining, J. (2007). Capillary pressure for the sand-CO_2-water system under various pressure conditions. Application to CO_2 sequestration. *Advances in Water Resources*, *30*(11), 2339–2353. https://doi.org/10.1016/j.advwatres.2007.05.010

Raeesi, B., Morrow, N. R., & Mason, G. (2014). Capillary pressure hysteresis behavior of three sandstones measured with a multistep outflow-inflow apparatus. *Vadose Zone Journal*, *13*(3). https://doi.org/10.2136/vzj2013.06.0097

Rasmusson, K., Rasmusson, M., Tsang, Y., & Niemi, A. (2016). A simulation study of the effect of trapping model, geological heterogeneity, and injection strategies on CO_2 trapping. *International Journal of Greenhouse Gas Control*, *52*, 52–72. https://doi.org/10.1016/j.ijggc.2016.06.020

Robins, V., Saadatfar, M., Delgado-Friedrichs, O., & Sheppard, A. P. (2015). Percolating length scales from topological persistence analysis of micro-CT images of porous materials. *Water Resources Research*, *52*(1), 315–329. https://doi.org/10.1002/2015WR017937

Roof, J. (1970). Snap-off of oil droplets in water-wet pores. *Society of Petroleum Engineers Journal*, *10*(01), 85–90. https://doi.org/10.2118/2504-PA

Ruprecht, C., Pini, R., Falta, R., Benson, S., & Murdoch, L. (2014). Hysteretic trapping and relative permeability of CO_2 in sandstone at reservoir conditions. *International Journal of Greenhouse Gas Control*, *27*, 15–27. https://doi.org/10.1016/j.ijggc.2014.05.003

Saeedi, A., & Rezaee, R. (2012). Effect of residual natural gas saturation on multiphase flow behavior during CO_2 geo-sequestration in depleted natural gas reservoirs. *Journal of Petroleum Science and Engineering*, *82–83*, 17–26. https://doi.org/10.1016/j.petrol.2011.12.012

Schlüter, S., Berg, S., Rücker, M., Armstrong, R., Vogel, H.-J., Hilfer, R., & Wildenschild, D. (2016). Pore-scale displacement mechanisms as a source of hysteresis for two-phase flow in porous media. *Water Resources Research*, *52*(3). 2194–2205. https://doi.org/10.1002/2015WR018254

Sheppard, A. P., Sok, R. M., & Averdunk, H. (2004). Techniques for image enhancement and segmentation of tomographic images of porous materials. *Physica A: Statistical Mechanics and its Applications*, *339*(1), 145–151. https://doi.org/10.1016/j.physa.2004.03.057

Shi, J.-Q., Xue, Z., & Durucan, S. (2011). Supercritical CO_2 core flooding and imbibition in Berea sandstone-CT imaging and numerical simulation. *Energy Procedia*, *4*, 5001–5008. https://doi.org/10.1016/j.egypro.2011.02.471

Shukla, R., Ranjith, P., Haque, A., & Choi, X. (2010). A review of studies on CO_2 sequestration and caprock integrity. *Fuel*, *89*(10), 2651–2664. https://doi.org/10.1016/j.fuel.2010.05.012

Singh, K., Bijeljic, B., & Blunt, M. J. (2016). Imaging of oil layers, curvature, and contact angle in a mixed-wet and a water-wet carbonate rock. *Water Resources Research*, *52*(3), 1716–1728. https://doi.org/10.1002/2015WR018072

Singh, K., Menke, H., Andrew, M., Lin, Q., Rau, C., Blunt, M. J., & Bijeljic, B. (2017). Dynamics of snap-off and pore-filling events during two-phase fluid flow in permeable media. *Scientific Reports*, *7*(1), 5192. https://doi.org/10.1038/s41598-017-05204-4

Song, J., & Zhang, D. (2013). Comprehensive review of caprock-sealing mechanisms for geologic carbon sequestration. *American Chemical Society*, *47*(1), 9–22. https://doi.org/10.1021/es301610p

Succi, S. (2001). *The lattice Boltzmann equation: For fluid dynamics and beyond*. Clarendon Press.

Sun, C., McClure, J. E., Mostaghimi, P., Herring, A. L., Berg, S., & Armstrong, R. T. (2020). Probing effective wetting in subsurface systems. *Geophysical Research Letters*, *47*(5), e2019GL086151. https://doi.org/10.1029/2019GL086151

Sun, C., McClure, J. E., Mostaghimi, P., Herring, A. L., Meisenheimer, D. E., Wildenschild, D., et al. (2020). Characterization of wetting using topological principles. *Journal of Colloid and Interface Science*, *578*, 106–115. https://doi.org/10.1016/j.jcis.2020.05.076

Sun, C., McClure, J. E., Mostaghimi, P., Herring, A. L., Shabaninejad, M., Berg, S., & Armstrong, R. T. (2019). *Linking continuum-scale state of wetting to pore-scale contact angles in porous media*. Retrieved from http://arxiv.org/abs/1910.00484

Tanino, Y., & Blunt, M. J. (2012). Capillary trapping in sandstones and carbonates: Dependence on pore structure. *Water Resources Research*, *48*(8). https://doi.org/10.1029/2011WR011712

Tokunaga, T. K., Wan, J., Jung, J.-W., Kim, T. W., Kim, Y., & Dong, W. (2013). Capillary pressure and saturation relations for supercritical CO_2 and brine in sand: High-pressure $P_c(S_w)$ controller/meter measurements and capillary scaling predictions. *Water Resources Research*, *49*(8), 4566–4579. https://doi.org/10.1002/WRCR.20316

Wan, J., Kim, Y., & Tokunaga, T. K. (2014). Contact angle measurement ambiguity in supercritical CO_2-water-mineral systems: Mica as an example. *International Journal of Greenhouse Gas Control*, *31*, 128–137. https://doi.org/10.1016/j.ijggc.2014.09.029

Wang, S., Edwards, I. M., & Clarens, A. F. (2013). Wettability phenomena at the CO_2-brine-mineral interface: Implications for geologic carbon sequestration. *Environmental Science & Technology*, *47*(1), 234–241. https://doi.org/10.1021/es301297z

Wang, S., Tao, Z., Persily, S. M., & Clarens, A. F. (2013). CO_2 adhesion on hydrated mineral surfaces. *Environmental Science & Technology*, *47*(20), 11858–11865. https://doi.org/10.1021/es402199e

Wang, S., & Tokunaga, T. K. (2015). Capillary pressure-saturation relations for supercritical CO_2 and brine in limestone/dolomite sands: Implications for geologic carbon sequestration in carbonate reservoirs. *Environmental Science & Technology*, *49*(12), 7208–7217. https://doi.org/10.1021/acs.est.5b00826

Wildenschild, D., Armstrong, R. T., Herring, A. L., Young, I. M., & William Carey, J. (2011). Exploring capillary trapping efficiency as a function of interfacial tension, viscosity, and flow rate. *Energy Procedia*, *4*, 4945–4952. https://doi.org/10.1016/j.egypro.2011.02.464

Zhang, X., Ge, J., Kamali, F., Othman, F., Wang, Y., & Le-Hussain, F. (2020). Wettability of sandstone rocks and their mineral components during CO_2 injection in aquifers: Implications for fines migration. *Journal of Natural Gas Science and Engineering*, *73*, 103050. https://doi.org/10.1016/j.jngse.2019.103050

Zuo, L., & Benson, S. M. (2014). Process-dependent residual trapping of CO_2 in sandstone. *Geophysical Research Letters*, *41*(8), 2820–2826. https://doi.org/10.1002/2014GL059653